UNIVERSITY OF CALIFORNIA,
IRVINE

Conformal Wearable Electronics: Towards Ubiquitous Physiological Monitoring

DISSERTATION

submitted in partial satisfaction of the requirements for the degree of

DOCTOR OF PHILOSOPHY

in Biomedical Engineering

by

Lancy Lin

Dissertation Committee:
Professor Michelle Khine, Chair
Professor Abraham P. Lee
Professor William C. Tang

2020

DEDICATION

To

My parents Liang Dong Lin and Sharon Lin

&

My siblings Kimberly Lin, Amy Lin, and Raymond Lin

Table of Contents

LIST OF FIGURES

LIST OF TABLES

ACKNOWLEDGEMENTS

I would like to express my sincerest gratitude to my academic advisor Professor Michelle Khine for all her guidance and offers of personal support. Michelle is the reason I applied for the graduate program at UC Irvine. I remember attending one of her research seminars and was instantly hooked by her research and creativity. My enthusiasm was well-warranted when she agreed to advise me. At many points of my graduate studies, Michelle provided positive perspectives that encouraged me to persist through research uncertainties. She is the academic epitome of a super woman, and it has truly been my privilege to be a member of the Khine Lab.

I would like to thank my committee members: Dr. Abraham Lee, Dr. William Tang, Dr. Weian Zhao, and Dr. Gillian Hayes. Their thoughtful advice and constructive criticism helped shape my thesis proposal. I also greatly appreciate their friendliness and approachability. I find it rare for a professor to remember me after one meeting. Years later, it is even more rare to be able to chat and engage in light banter.

I would like to thank my collaborators: Dr. Dawn Lombardo, Dr. Weian Zhao, Dr. Shaista Malik, Dr. Peter Tseng, Manik Dautta, Amirhossein Hajiaghajani, Alberto Escobar, and Cody Dunn. This dissertation greatly lends to their expertise and willingness to invest their time.

I would like to thank the members of the Khine Lab for their collaborative spirits and emotional support. I would like to recognize Himanshu Sharma for energetically inviting me into the lab on my first visit; Joshua Kim, Eugene Lee, Sophia Lin, Jolie Nokes, and Jonathan Pegan for their mentorship; Michael Chu and Thao Nguyen for our cohort companionship; and everyone I had the opportunity to collaborate and learn from. I have great memories about the jumping competitions and photography lessons that took place in the lab.

I would like to thank my mentors and colleagues: Dr. Gisela Lin, Linda McCarthy, Ann Fain, Alvin Viray, Sally Avila, and everyone else at the BME office. I would also like to express my gratitude to everyone I met at Beckman Coulter during my industry internship. It was a wonderful experience and completely worth the accrued mileage.

I would like to thank my classmates and friends. I abstain from naming you individually because that would significantly lengthen this acknowledgements page, and risk forgetting to name others. I hope you know your friendship, humor, and advice have supported me through the tough points of graduate school and life events. You know who you are!

Finally, I would like to bring the world to my family. My parents Sharon and Liang were first-generation immigrants and shed blood, sweat, and tears to support a family of four children. My siblings and I share a life of gratitude for their ethics and hard work. It is my honor to dedicate the first doctoral degree in the family to them.

CURRICULUM VITAE

Lancy Lin

2020 **PhD**, University of California, Irvine
Biomedical Engineering
Thesis: Conformal Wearable Electronics for Ubiquitous Physiological Monitoring
2017 **MS**, University of California, Irvine
Biomedical Engineering
2013 **BS**, University of California, San Diego
Bioengineering - Biotechnology

PUBLICATIONS

L. Lin, M. Dautta[2], A. Hajiaghajani[2], A.E. Escobar, P. Tseng, M. Khine **Paint-on epidermal electronics for on-demand sensors and circuits** Advanced Electronic Materials. (2020)

L. Lin[1], J.A. Zakashansky[1], Y. Zhou[1], M. Khine **Band-Aid©-like wearable strain-based electrogoniometer for monitoring knee joint rehabilitation** *In preparation*

L. Lin, M. Chu, S.-J. Park, J.A. Zakashansky, M. Khine **Conformal stretch sensors for high-resolution motion sensing and control** Macromolecular Materials and Engineering. 304(2017)

S. Li, L. Lin, X. Chang, Z. Si, K. Plaxco, M. Khine, H. Li, F. Xia **A wrinkled structure of gold film greatly improves the signaling of electrochemical aptamer-based biosensor** *Submitted to RSC Advances*

M. Sprowls[1], M. Serhan[1], E.-F. Chou, L. Lin, C. Frames, I. Kucherenko, K. Mollaeian, Y. Li, V. Jammula, D. Logeswaran, M. Khine, Y. Yang, T. Lockhart, J. Claussen, L. Dong, J.J.-L. Chen, J. Ren, C. Gomes, D. Kim, T. Wu, J. Margrett, B. Narasimhan, E. Forzani **Integrated sensing systems for monitoring interrelated physiological parameters in young and aged adults** *Submitted to International Journal of Prognostics and Health Management*

A. Imamura[1], J.A. Zakashansky[1], K. Cho, L. Lin, E. Carrilho, M. Khine **Stretchable sensors for nanomolar glucose detection** Advanced Materials Technologies. 5(2020)

ORAL PRESENTATIONS

L. Lin, D. Oyarzun, J. Santiago, M. Khine "Rapid Nucleic Acid Purification and Sequence-specific Detection for Agricultural Applications," Center for Advanced Design and Manufacturing of Integrated Microfluidics (CADMIM) IAB Conference, Cincinnati, Ohio, September 2016

L. Lin, S.-J. Park, J.D. Pegan, M. Khine "Stretchable Electronics Enhanced with Highly Wrinkled Metal Thin Films," SoCal Micro and Nanofluidics Symposium, Irvine, California, September 2016

POSTER PRESENTATIONS

L. Lin, J.A. Zakashansky, Y. Zhou, M. Chu, M. Khine, "Stretchable Sensors for Human Motion Sensing and Control," EMBS Micro and Nanotechnology in Medicine Conference, Kauai, Hawaii, 2018

M. Chu, J. Kim, L. Lin, E.-F. Chou, T. Nguyen, M. Khine, "Honey, We Shrunk Healthcare: Continuous Physiological Monitoring," Center for Advanced Design and Manufacturing of Integrated Microfluidics (CADMIM) Annual Meeting, Irvine, California, March 2019

J.A. Zakashansky, A.H. Imamura, L. Lin, M. Khine, "40-Fold Increase in Electrochemically Active Surface Area on Wearable Shrink Electrodes," Center for Advanced Design and Manufacturing of Integrated Microfluidics (CADMIM) Annual Meeting, Irvine, California March 2019

M. Chu, L. Lin, T. Nguyen, M. Kim, E. Lee, J. Morival, M. Khine, "Ditch the Lid: Reversible and Open-Channel Microfluidics," Center for Advanced Design and Manufacturing of Integrated Microfluidics (CADMIM) Annual Meeting, Irvine, California, March 2017

M.Y. Kim, L. Lin, M. Chu, J. Morival, A. Siddiqui, J. Nokes, M. Khine, "Superhydrophobic Microfluidics," Center for Advanced Design and Manufacturing of Integrated Microfluidics (CADMIM) Annual Meeting, Irvine, California, March 2016

J. Kim, J.D. Pegan, S.-J. Park, L. Lin, M. Chu, M. Khine, "Highly Stretchable, Skin-Like Sensors and Electronic Components," Center for Advanced Design and Manufacturing of Integrated Microfluidics (CADMIM) Annual Meeting, Irvine, California, March 2016

PATENTS

U.S. Patent 10,780,688: "Highly Wrinkled Metal Thin Films Using Lift-off Layers," September 22, 2020

Application: "Conductive Inks Using Craft Glue," Provisional filed November 25, 2020

HONORS AND AWARDS

2019 1st Place, UC Irvine Beall Student Design Competition
2018 Fellow, National Science Foundation Non-Academic Research Internships
2018 Fellow, Public Impact Fellowship

2017 3rd Place, MicroTAS Convention Shark Tank Competition
2015 Honorable Mention, NSF Graduate Research Fellowship
2014 Honorable Mention, NSF Graduate Research Fellowship
2014 Awardee, Edwards Lifesciences Scholarship for Medical Device & Investor Forum

CERTIFICATIONS

2020 Certificate of Remote Instruction on Evidence-Based Pedagogy
2014 NCEES Engineer-in-Training (EIT) #153756

ABSTRACT OF THE DISSERTATION

Conformal Wearable Electronics: Towards Ubiquitous Physiological Monitoring

by

Lancy Lin

Doctor of Philosophy in Biomedical Engineering

University of California, Irvine, 2020

Professor Michelle Khine, Chair

Wearable electronics provide valuable insights into physiological health, sports performance, and disease management. They continually evolve to become more epidermal-like, yet still face challenges pertaining to conformity, sensitivity, profile, and reliance on wires and power sources. These factors impact their wearability and compatibility for ambulatory monitoring. For more versatile and robust physiological monitoring, there is a need to improve the current electronic features towards more ubiquitous modalities. The work presented here focuses on multi-faceted improvements of conformal wearable electronics, including a method for producing highly sensitive and stretchable strain sensors. The improved sensors can withstand significant mechanical strain over joints while providing high-resolution measurements of joint flexion. A system of physiological monitors is tested in IRB-approved pilot studies in efforts to discover pertinent digital biomarkers vital to the early detection and management of cardiovascular diseases. A skin-safe conductive ink made from commodity school glue addresses the need for on-demand and highly conformal epidermal dry electronics. Finally, temporary tattoo electronics made from the conductive ink are demonstrated for wireless and battery-free operation via NFC linkage.

CHAPTER 1: Introduction

1.1 Motivation

In the age of peer-to-peer connectivity and increasing awareness of personal and communal health, wearable technologies are vital components of modern human physiological monitoring. The rapid growth in the field has generated an influx of research dedicated to improving the wearability, sensitivity, and profile of the electronics for personal and ambulatory usage.[1] As a result, wearable electronics are evolving to be increasingly portable and personalized.

Many commercially available wearable electronics suffer from obtrusive and non-conformal designs. Factors that limit conformity and comfort of wear include planar and rigid components, wire connections, or bulky components including batteries.[2] Common examples of obtrusive wearable devices on the market include blood pressure cuffs, electrocardiogram (ECG) monitors, and smart activity monitors (Apple Watch, Fitbit Charge, Amazon Halo, etc.).[3–5] These devices enable users to track their health over discrete time periods, but the biometric information they provide is limited by their rigidity and form factor.

Modalities that address the conformity of physiological monitors can be classified under wearable textiles, flexible/stretchable sensors, and conductive paints. Wearable textiles place compressive force on embedded sensors and wires are uncomfortable for long periods of wear.[4,6] Flexible and stretchable sensors utilize thin functional materials, strain-relieving features, and soft/stretchable polymer support layers, but often compromise measurement sensitivity for stretchability.[7–9] Conductive paints can be painted directly onto the skin to achieve maximal conformity, but can suffer from brittleness when dried or low skin compliance from ink

toxicity.[10–12] Depending on the desired applications and features, different modalities can be chosen to achieve specific wearable advantages.

Progress towards conformal wearable technologies is also constrained by bulky and rigid power sources and discrete communication modules (e.g. Bluetooth) necessary for the capture and transmittance of physiological data.[9,13,14] Off-the-shelf components like communication antennas and resonant coils can be connected to the electronics to achieve battery-free and wireless status, but the strategy of connecting dissimilar components require the electronics to operate with bulk connective housing.[15,16] The connections complicate their manufacturing and scalability. They also add potential device failure points wherever stiffness mismatches exist between the rigid connectors and more conformal electronics.

Wearable electronics also benefit from downstream integrative compatibility. Individual sensors can detect a limited category of single-variable physiological data, but a system of sensors can record single- and multi-variable data. For example, Chu *et al.* used piezo-resistive strain sensors to record respiration from thoracic expansion, and then integrated the cyclical inhalation curve to calculate respiration volume.[14] Kim *et al.* used capacitive pressure sensors to detect the pulsatile waveform from the radial artery, and then calibrated the waveform to output blood pressure information.[13] Both sensor types are capable of non-invasive continuous recording of physiological data, and share comparable form factors and elastic moduli. If the respiration and blood pressure sensors can be integrated, then the jointly collected data can be analyzed for cardiopulmonary multi-variable and symbiotic factors. In cardiovascular disease studies, hemodynamic and respiration digital biomarkers can offer clues to disease progression or prognosis.[17–19] The ability to combine multiple wearable electronics into comprehensive monitoring systems increases the likelihood of collecting clinically relevant datasets.

Conformal wearable electronics have greatly advanced since their conception, but various motifs still face design challenges that limit their ubiquitous usability.[1,20] There remains a need to continuously improve the conformity, performance, and clinical relevance of wearable technologies for applications that require higher standards of sensitivity, dynamic range, comfort, and portability. Strategies and methods for maximizing the advantageous characteristics of various wearable electronic motifs will be discussed in this work.

1.2 Overview of dissertation

The dissertation is structured as follows. Chapter 2 introduces a wearable strain sensor that exhibits high stretchability without trading sensitivity to mechanical strain. In Chapter 3, the shape memory polymer (SMP)-based strain sensors are demonstrated for their wearability over high-straining joints and high-resolution measurements of joint angle. Chapter 4 applies a set of conformal wearable sensors for more comprehensive human physiological monitoring in healthy and medically impaired individuals. Two pilot studies examine for potential digital biomarkers of cardiovascular diseases (CVD) for prevention and disease management. Chapter 5 describes a novel conductive ink formula using children's school glue as the basis for paint-on epidermal electronics. The ink can be fashioned into on-demand dry electrodes for detecting electrophysical and electrodermal activities. Temporary tattoo-like devices made from the ink can communicate under radiofrequency (RF) bands for wireless and battery-free operation of sensors and circuit components. Chapter 6 concludes this work with a discussion of the future directions of wearable electronics towards ubiquitous physiological monitoring.

CHAPTER 2: Sensors with improved sensitivity and stretchability

2.1 Introduction

A key criterion of wearable electronics is the compatibility with the intended user. Compatibility can be assessed by answering the following two questions: Does the electronic perform its intended purpose on the wearer? Does it conflict with the native performance of the wearer? If compatibility is accessed on a wearable sensor, then the criterion narrows down to whether the sensor can sense its intended target without impeding nor being impeded by body motion. In short, an ideal sensor can perform its intended task and perform it well without obtrusion.

Motion sensors such as accelerometers are relatively commonplace today, finding homes in cars, cellular phones, watches etc. While these conventional sensors can capture motion, whether they can repeatably capture high resolution motion while being worn by a user remains questionable. Applications that require quantitative monitoring such as fitness and athletic performance, gesture control for virtual or augmented reality control, and feedback for prosthetics and physical rehabilitation would greatly benefit from highly sensitive and stretchable sensors.[21–23] These sensors must be sufficiently conformal to be unobtrusively applied to the skin in order to track fine movements with high resolution.

For compatibility with wearable applications and high signal resolution, it is imperative that motion sensors are not only flexible but also stretchable while maintaining high sensitivity to strain across a large dynamic range. Piezoresistive-type strain sensors can potentially fulfill this task. These sensors translate mechanical deformation (e.g. flexion or strain) into electrical changes. For a strain sensor, the known relationship between the amount of strain and its associated change

in electrical resistance can be characterized as the gauge factor (GF), or sensitivity of the sensor (**Eq. 1**):

$$GF = {}^{\Delta R/R_0}/_{\varepsilon} \qquad (1)$$

where $\Delta R/R_0$ is the normalized change in resistance and ε is the strain.

The adoption of stretchable elastomer substrates in sensors has advanced the development of stretchable and conformal sensors. But the trade-off between dynamic range and sensitivity remains a persistent challenge. To achieve a large dynamic range without decreasing sensitivity, skin-mountable stretch sensors have been fabricated using pre-stressed shape memory polymer (SMP) platforms. The SMPs produce a stiffness mismatch between the deposited film of a specified functional material and the underlying SMP (namely polystyrene (PS)) substrate during the shrinking process, causing the thin film to buckle and form wrinkles.[24] Transition from the SMP platform to the finished strain sensors is achieved by lifting the wrinkled thin film off the SMP substrate and transferring it onto an elastomeric substrate with an elastic modulus similar to that of skin. The finished sensors contain stress-relieving wrinkle features that delocalize microfracture formation and prolong fracture propagation. The presence of stress-delocalizing wrinkles aims to address the strain sensor caveat in two ways: 1) dynamic range is increased because the wrinkle morphology aids stress relief during fracture nucleation and elongation and extends the conductivity range, and 2) sensitivity can be increased by tuning the film thickness, changing the geometric structure and form factor, or opting for functional materials with large Young's moduli (e.g. more brittle materials).[1,9,25–27] Such is the case for Pegan *et al.* in which a stretchable strain sensor comprised of a shrink-induced wrinkled bimetallic Pt:Au (PS-bimetallic) thin film and hairpin loop design achieved a dynamic range of 185% and reported a maximum sensitivity of GF=42; the trendline sensitivity of the linear response region (henceforth called

"linear sensitivity") was GF~6.[9] In comparison, Au-only stretchable thin film (PS-Au) wires fabricated with the same shrinkable PS substrate achieved a slightly larger dynamic range of 200% (due to Au-only being more malleable than Pt:Au) but exhibited poor sensitivity as low as GF=0.087.[28] Zhu and Moran-Mirabal coupled the SMP platform with a lift-off process to fabricate PS-Au type sensors with improved sensitivity (GF~0.75), but the dynamic range was reduced to 135% strain due to film delamination.[27] It is important to note that the linear range of both the PS-Pt:Au and PS-Au were limited to approximately 0-50% strain, which makes less compatible for applications with larger dynamic needs (e.g. joint and limb motion). Sensors made with wrinkled films of percolating carbon nanotube (PS-CNT) networks have achieved dynamic ranges of over 700% with a linear range of 0-400% strain, but also have low linear sensitivity of GF=0.67.[29] The CNT-based sensors are also disadvantageous because nanoparticles pose as respiratory hazards and lack biocompatibility with cellular systems.[30] CNTs and other conductive particles like graphene nanoflakes can be absorbed or directly mixed into elastomers to create stretchable sensors with reduced airborne risks.[31,32] Three-dimensional porous electrodes made by mixing CNT into silicone achieve GF=134 and a working range up to 160% strain.[33] But this strategy significantly increases the amount of required conductive material and makes them more expensive to fabricate.

This chapter addresses the need for stretchable and sensitive sensors for high resolution motion sensing and control. Prior work has shown that Shrinky-Dink®-based technologies add strain-relieving wrinkle features. The use of a new type of shrinkable polymer yields additional shrinkage and subsequent improvements in both stretchability and sensitivity without compensatory advantage. The result is strain sensors with initial resistance as low as 300 Ω, enhanced dynamic range up to 368%, and a linear sensitivity as high as GF=9.6 from 0-150%

strain.[34] The excellent linear response and smaller footprint due to greater shrinkage makes them attractive for high strain applications like precision monitoring or motor control of joints in areas with limited real estate. Compatibility of the lift-off process with roll-to-roll manufacturing techniques adds low-cost and scalability to the sensors.[35]

2.2 Material and design parameters

2.2.1 Fabrication platform

Given that current PS stretch sensors have achieved greater dynamic range via shrink-induced stress-delocalizing wrinkles, it is logical that greater shrinkage will produce more wrinkle formation and can result in even greater dynamic range. Commodity shrink-wrap film comprised of polyolefins (PO), another type of SMP, shrinks by 95% in area and generates a greater compression force than PS (66% area reduction).[24,36]

PO shrinkage has benefited the generation of microstructure templates, platforms with optical or fluorescence signal enhancements, increased electrochemically-active surface area, and chemical-free superhydrophobic surfaces.[24,37–42] But due to its relative chemical resistance against common solvents, the lift-off of wrinkled metal thin films from PO cannot be achieved in the same fashion as PS lift-off. For this reason, a dissolvable sacrificial layer is chosen as the intermediary between the PO and deposited metal layers. The sacrificial layer selection is detailed in Section 2.4.1.

2.2.2 Functional material

The function material determines the electrical, mechanical, and chemical properties of the sensor. Conductive materials compatible with thin film deposition systems include platinum (Pt),

gold (Au), silver (Ag), copper (Cu), nickel (Nu), and titanium (Ti). For conductive stability, metals that do not readily oxidize (Pt, Au, Ag) are favorable. Pt is a relatively brittle metal, making it a suitable choice for high-sensitivity piezo-resistive strain sensors.[9] Au is more malleable and less probe to stress fractures, making it suitable for low-resistance wires.[28] Sections 3.5.1 and 3.5.2 describe the morphology and characterization of Pt-based strain sensors. Due to the specificity of the body chemistry towards Au and the elastomer, a layer of Au added between the Pt and elastomer, forming a bimetallic Pt:Au thin film. Section 3.5.3 describes the characterization of PO-based wires.

2.2.3 Support substrate

Since the introduction of epidermal electronics in 2011, soft and flexible materials such as silicone and textiles have increasingly been incorporated into wearable electronics.[20] Silicones are preferrable for on-skin wear due to similar elastic moduli as native skin.[43] Poly(dimethyl)siloxane, or PDMS, can provide flexibility and skin-like texture to wearable electronics, but its relative material stiffness complicates their compatibility for high-strain applications such as joint monitoring.[44] Alternatively, Ecoflex 00-30 (Smooth-On) can achieve up to 900% strain and has already been incorporated with SMP-based highly stretchable strain sensors and wires.[9,28]

2.2.4 Sensor geometry

The 2D geometry of the sensor functional and support materials can enhance the stretchability and sensitivity of a strain sensor. Kim *et al.* added serpentine patterns to the functional layer to add strain tolerance up to 30%.[20] Meanwhile, Pegan *et al.* incorporated hairpin loop patterns to lengthen the electrical path and add more fracture points in effort to increase

sensitivity.[9] To fairly compare the performance of PO-based sensors to PS-based sensors, the characterization of the PO sensor sensors is performed with the simple straight-trace designs.

2.4 Lift-off technique

2.4.1 Sacrificial layer material

Due to the chemical resistivity of PO relative to PS, a sacrificial layer susceptible to solvent dissolution was incorporated into the sensor fabrication process.[45] Prior to the metal deposition step, a layer of sacrificial material was coated onto the PO film to later enable lift-off of the wrinkled metal thin film. Various sacrificial materials were investigated ranging from liquid resins (e.g. wet- or dry-erase ink) to liquid polymers. Early trials of sacrificial layers were unsuccessful due to heat-induced crystallization from the shrinking process. The crystallization increased the brittleness of the sacrificial layer, leading to undesired fragmentation of the metal layer.

A preliminary sacrificial layer that attained moderate transfer success was PS dissolved in toluene at concentrations ranging from 1-5% by weight. The dissolved PS was spun-coated onto sheets of PO at 1000 rpm for 30 seconds. Under a 3D confocal laser microscope (Keyence VK-X100), it was observed that higher percentages of PS produced wrinkles with larger wavelengths. Higher percentages of PS, when spun at the same rate, deposited thicker sacrificial layers and increased the overall deposition thickness. The thicker material generated a larger stiffness mismatch between the deposited materials and the shrinking PO and reduced the wrinkling ability of the deposited metal layer (**Figure 2.1**). Notably, the thermally induced shrinking process did not induce metal film fracture. From investigation, it was determined that the PS and PO shared similar glass transition temperatures, enabling the PS layer to reflow with the wrinkling process while the PO underwent shrinkage. From this discovery, it was determined that the ideal sacrificial

layer for PO would behave similarly to PO under heat treatment, namely a thermoplastic material with a similar glass transition temperature.

After several trials, the choice sacrificial material was found to be poly(methyl)methacrylate (PMMA). Dissolved PMMA with a molecular weight (MW) of 950 kDa (MicroChem 950 PMMA A2), commonly used as photoresist, was chosen due to its commercial availability, documented ability to produce thin layers, reflow properties (similar glass transition temperature), and high susceptibility to acetone dissolution. Also, the PMMA was resistant to crystallization and oxidation that could arise from the plasma-induced metal deposition.

2.4.1 Fabrication and transfer process

Pre-stressed polyolefin (PO) films (Sealed Air, Nexcel multilayer shrink film 955D) were affixed to glass slides using ethyl alcohol (EtOH) and polyimide tape (Kapton) to provide compatible mechanical support for standard micromachining equipment. The PO film was coated with PMMA (MicroChem, 950 PMMA A2) as a sacrificial layer at 1000 rpm for 40 sec and air-dried overnight under ventilation.

Sensor designs were drawn using computer-aided design software (Autodesk). The sensor design was laser machined (Versa Laser, VLS2.30) onto a single-sided adhesive polymer mask (Grafix Arts, Frisket Film). The mask was adhered onto the coated PO film. For ease of characterization, sensors were fabricated using a straight trace design flanked by connection pads (see **Figure 2.2**).

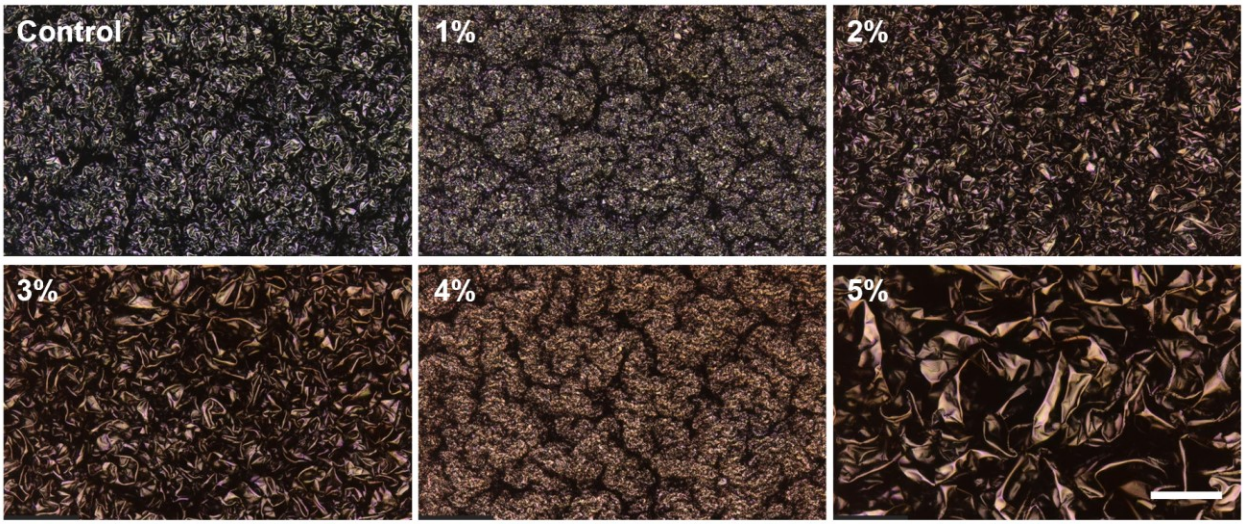

Figure 2.1 Effect of sacrificial layer thickness on wrinkle morphology. Polystyrene (PS) was dissolved in toluene at 1-5% by weight and spun-coated onto polyolefin (PO) prior to metal deposition and shrinkage. Higher concentrations produce thicker sacrificial layers, which results in larger wrinkle wavelengths. Scale bar is 25 μm.

Depending on the desired sensitivity, the following materials were deposited on the masked PO film using a timed magnetron sputter deposition (Quorum Technologies, Q150R). For highly sensitive strain sensors, a 5 nm Pt thin film was deposited for 207 sec, followed by a 5 nm Au thin film for 102 s to create a bimetallic thin film. For highly conductive stretchable wires, a 25 nm Au thin film was deposited for 500 sec. The sample was subsequently placed in a convection oven at 160 °C for 8 min between two parchment-lined glass plates. The sensor design was shrunk to 5% of its original size, generating wrinkles.

An adhesion promoter was used to reliably transfer the wrinkled thin film to an elastomer (Smooth-On, Ecoflex 00-30). The shrunken sample was treated with a 5 mM solution of (3-mercaptopropyl) trimethoxysilane in ethanol (Sigma Aldrich, 95% MPTMS) for 1 hr before air drying. The elastomer was promptly drop-casted over the sample until a thin complete coverage was achieved. The sample was placed under vacuum at 29 mmHg for 10 min. Afterwards, the sample was transferred to a 60 °C oven for 2 hr or until the elastomer was fully cured.

To dissolve the PMMA layer and achieve lift-off from the PO layer, the samples were placed in an acetone vapor chamber at 100 °C for 3 hr. A covered Erlenmeyer flask with the samples suspended within the neck of the flask was found to be the most efficient chamber shape. The narrow neck of the flask concentrated the rising acetone vapor, enabling faster dissolution of the sacrificial layer. Transfer was achieved once the sacrificial layer was fully dissolved, separating the wrinkled metal thin film and chemically bonded elastomer from the remaining PO layer. The transferred samples were immersed in an isopropanol bath for 20 mins to displace any residual acetone before drying overnight under ventilation. After dried, the sensors and wires were ready for testing and usage.

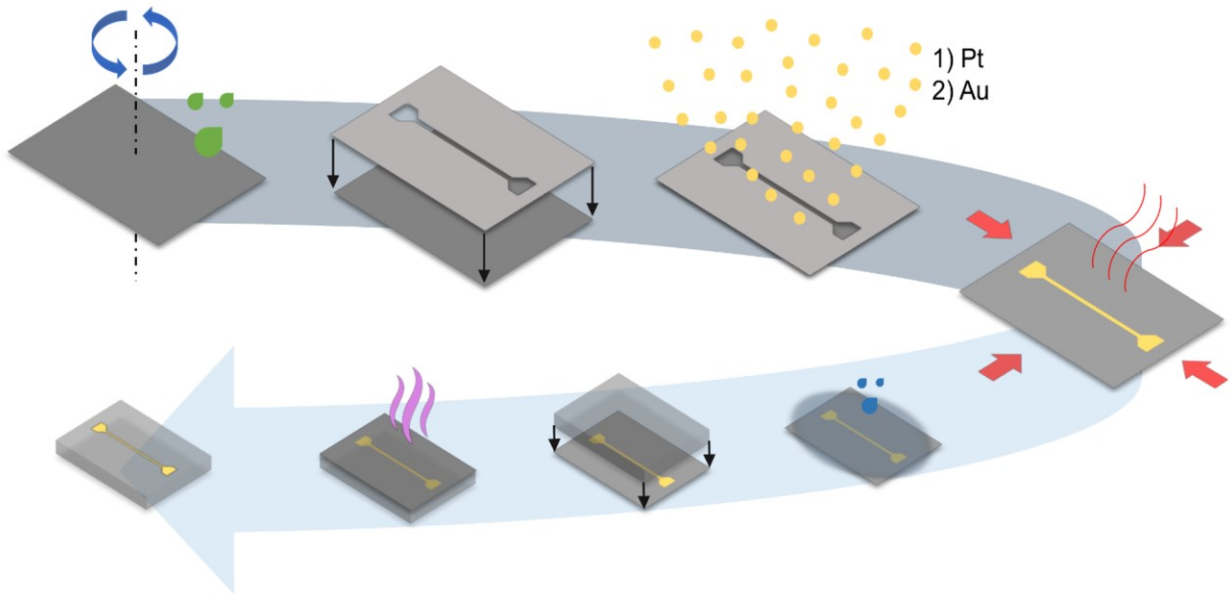

Figure 2.2 Fabrication process flow of the PO sensors. Steps beginning from top left: sacrificial layer coating, shadow mask application, metal thin film sputter deposition, thermal shrinkage, adhesion promoter treatment, elastomer casting, solvent vapor bath, and finished sensor.

2.5 Characterization

2.5.1 Bimetallic strain sensors morphology

Using the straight mask design with center trace dimensions of 2.50 mm width and 40.0 mm length, the final trace dimensions of the PO-bimetallic sensors were 590 μm ± 14 μm wide and 7.60 mm ± 0.11 mm long (n=8). For comparison, PS-bimetallic sensors were made from the same mask design and with the same metal deposition thickness. **Figure 2.3A-B** shows the size difference between sensors made from PO versus PS shrinkage.

The PO-bimetallic morphology was characterized under scanning electron microscopy (SEM) for the following conditions: as-deposited, post-shrinkage, post-transfer, and transferred with 200% strain (**Figure 2.4A**). A comparison of the post-shrinkage and post-transfer SEM images showed high fidelity of the wrinkles after the transfer process. Wrinkles were observed with wavelengths in the ~500nm (nano), ~5μm (micro), and ~20μm (meso) ranges, whereas the PS-bimetallic sensors exhibited only nano- and micro-wrinkles (**Figure 2.4B**). Prior literature on PS-based electronics had suggested that during the shrinking process, the more rigid metal film buckled and formed wrinkles until the highest density of nano-wrinkles was achieved; any remaining compression force went into forming the micro-wrinkles.[9] From this logic, the additional formation of meso-wrinkles in the PO-bimetallic sensors was likely due to an even greater excess of compression force that finished forming both the nano- and micro-wrinkles before entering the meso-wrinkle formation level.

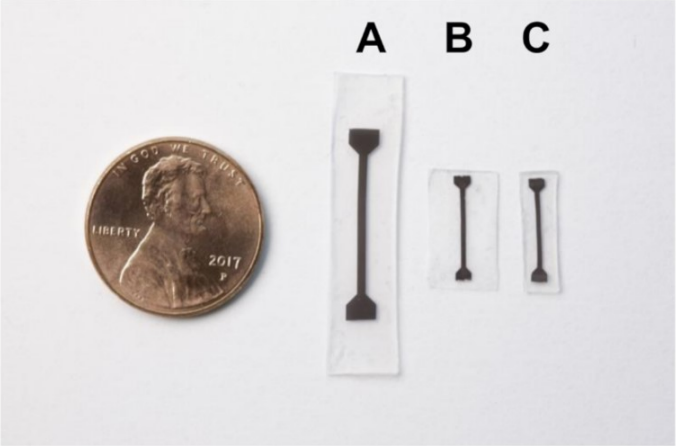

Figure 2.3 PS vs PO sensor shrinkage size. All sensors were made with the same design geometry. A) PS sensor. B) PO sensor with large elastomer substrate. C) PO sensor with small elastomer substrate.

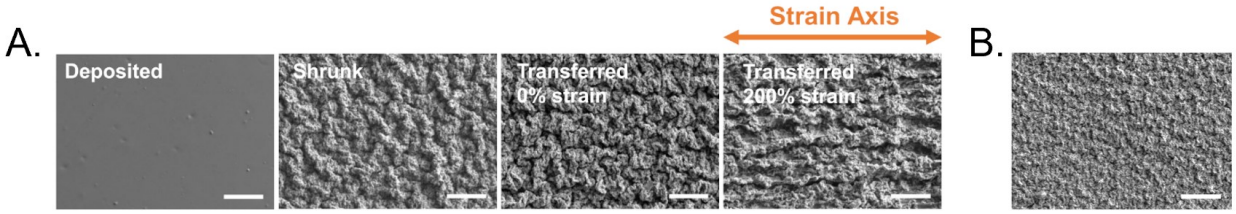

Figure 2.4 PO and PS wrinkle morphology under SEM. A) Various stages of the metal thin film on PO. Applied uniaxial strain expands the wrinkles in direction of motion. B) Compared to PO, the transferred PS sensor does not exhibit tertiary wrinkling.

2.5.2 Platinum strain sensors performance

The stretchability of the PO-bimetallic and PS-bimetallic sensors were tested by measuring their conductivity under strain until their strain-to-failure (STF) or break point (**Figure 2.5A-B**). Resistance changes across the sensor traces were converted to voltage and measured at 0.5 mm increments (PO~7% strain or PS~3.5% strain) using a two-probe setup, an automated linear stretching device with a strain rate of 12 mm s^{-1}, and a Wheatstone circuit. Each sensor was strained incrementally with 10-sec holds until their failure point at which gradual fracture elongation reached electrical disconnection. The average normalized change in resistance of each incremental hold was plotted against its respective strain percentage value. With the above testing conditions, the maximum achieved strain for the PO-bimetallic and PS-bimetallic sensors were 368% and

281%, respectively, supporting the theory that greater shrinkage results in greater stretchability. At publishing, this was the highest achieved dynamic range of a thin film piezoresistive strain sensor. The linear response range was found to extend from 0-150% for PO-bimetallic sensors whereas the PS-bimetallic sensors had a short linear range of 0-50%. This made the PO-bimetallic sensors very attractive for applications that require a large linear response range. A significant contribution to the enhanced dynamic range of the PO-bimetallic was the meso-wrinkles providing additional strain relief by unfurling along the axis of strain during the linear response phase of the STF test (see **Figure 2.4A**, transferred with 200% strain). The sensors exhibited similar strain response up to 100% strain. After 100% strain, they exhibited increased changes in resistance of varying magnitudes as they approached their STF points. Differences in the STF profiles after 100% strain were likely due to the natural variation of the fracture nucleation patterns. On a separate note, while the PS-bimetallic sensors did not strain as far as the PO-bimetallic, their dynamic ranges were significantly greater than Pegan *et al.*'s reported value of 185% strain.[9] This was likely due to upgrades of the vacuum equipment creating improved conditions of the polymer curing step, removing more trapped air from the wrinkle valleys and reducing the risk of film delamination during stretch testing. To determine if the sensor size influenced dynamic range, PO-bimetallic sensors with less Ecoflex surfaces area (width of ~3.7 mm instead of ~7.4 mm, see **Figure 2.3B-C**) were also tested. The ranges were found to be as much as 32% shorter (**Figure 2.6**). During stretch testing, it was observed that the edges of the Ecoflex parallel to the axis of strain would "bow" inward; this is explained by Poisson's ratio of Ecoflex = 0.49.[46] The "bowing" effect generated greater strain along the edges of the straight trace that encouraged faster fracture propagation, and this effect accelerated as the distance between the trace edge and Ecoflex edge decreased.

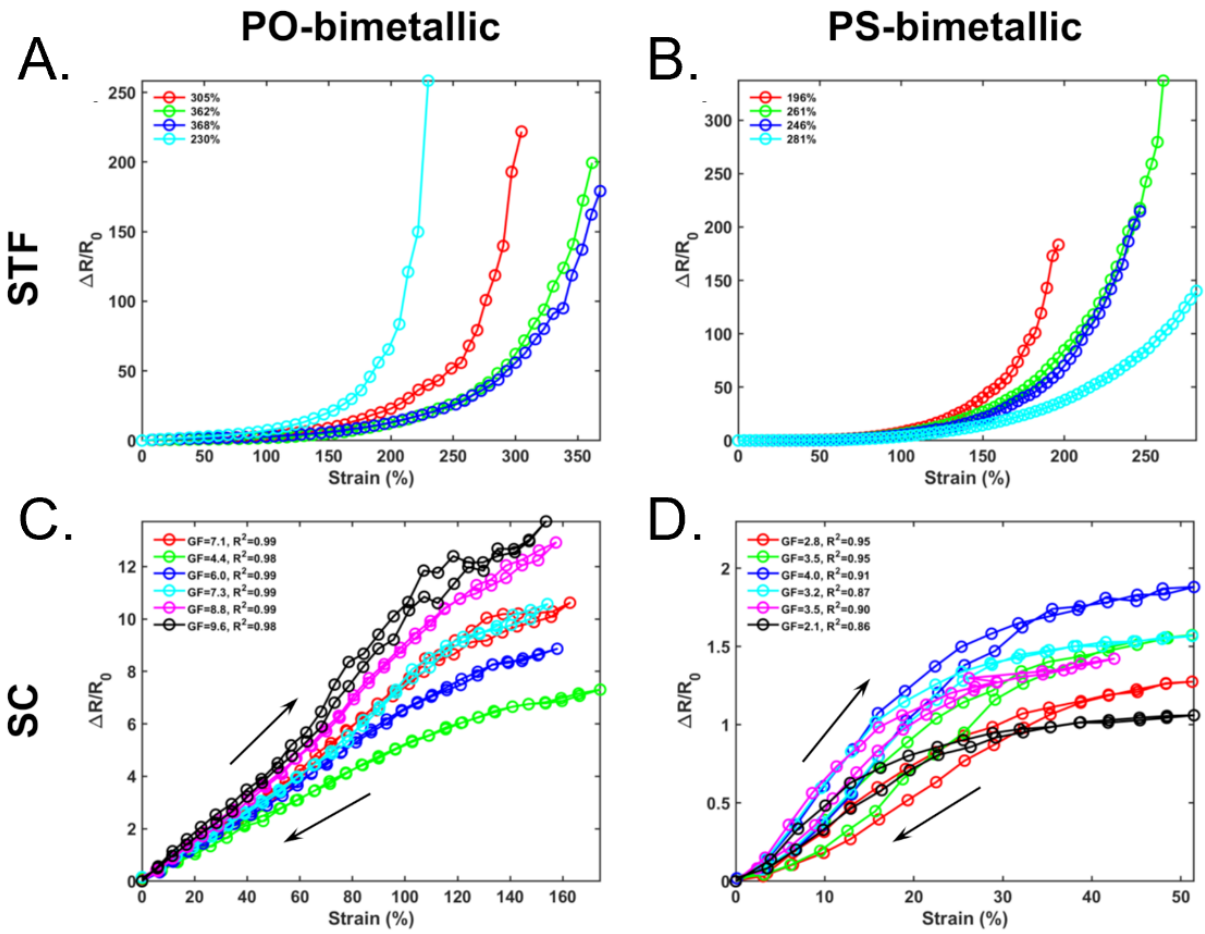

Figure 2.5 Stretchability and sensitivity of PO-bimetallic and PS-bimetallic sensors. A-B) Comparison of the dynamic range via STF testing (n=4 each). The linear response ranges of the STF curves were used to set the strain range of sensitivity testing C-D) Comparison of the sensitivity on pre-conditioned samples via cyclic testing. The PO sensors were strained from 0-150% whereas the PS sensors were strained from 0-50% (n=6 each). Note the comparatively low electrical hysteresis of the PO sensors.

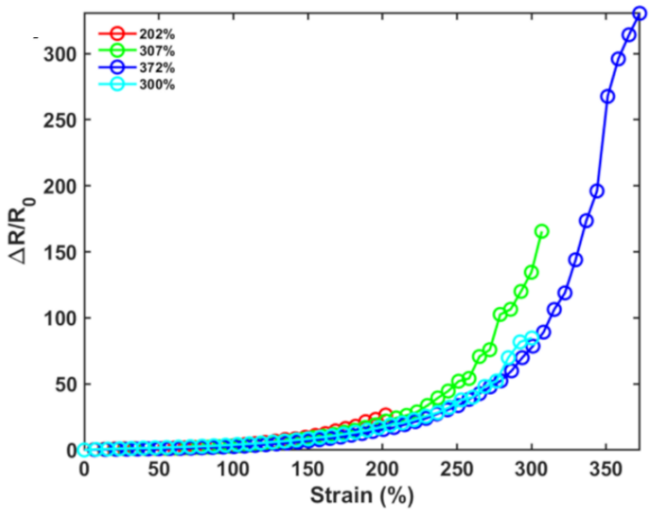

Figure 2.6 Effect of elastomer size on dynamic range. PO-bimetallic sensors with small elastomer substrate areas strained to failure earlier than those with larger substrate areas (data from Figure 2.5A).

To characterize the sensitivity to strain, conductivity of the sensors was measured at 0.5 mm strain increments using the same equipment setup and strain rate as the STF test. The tested range was chosen based on the maximum strain value exhibiting linear response to strain of the PO-bimetallic (150%) and PS-bimetallic (50%) sensors. Fresh sensors were pre-conditioned at 200% (PO-bimetallic) or 100% strain (PS-bimetallic) before undergoing three cycles of semi-static stretch and relaxation with 10-sec holds at each strain increment (one cycle is 0→linear max→0%). A linear curve was fitted to the third cycle of the normalized sensitivity data, and the slope of the fitted curve was taken as the GF (**Figure 2.5C-D**). The maximum linear GF of the PO-bimetallic and PS-bimetallic sensors were 9.6 and 3.5, respectively. It was noted that compared to the sensitivity of the linear response region from the STF test (GF<1), the GF from sensitivity testing was >10x greater. Only the sensors for the sensitivity tests were pre-conditioned, meaning that the fractures were already formed at the start of the sensitivity tests (higher, but more stable absolute resistance values due to less fracture elongation), whereas fractures were nucleating and elongating in the wrinkled thin film during the STF tests (lower absolute resistance values). After pre-conditioning, the PO-bimetallic sensors were approximately 2x more sensitive to strain than the

PS-bimetallic sensors. Given that the PO-bimetallic sensors were simple straight traces with already high sensitivity to strain, and the sensitivity of the PS-bimetallic sensors was approximately half the reported value of Pegan *et al.*'s sensors with a more complex design, the sensitivity of the PO-bimetallic sensors can be tuned higher by increasing the length-to-width ratio of the traces or adding hairpin loops to the trace geometry to increase the fracture density across a single plane.[9,27]

Cyclic curves of sensor stretch and relaxation allowed visualization of the electrical hysteresis of the sensors. The electrical hysteresis was defined as the difference in the areas under the stretch and relaxation curves; smaller differences equate to less hysteresis. The PO-bimetallic sensor curves were observed to overlap in most samples, thus the sensors exhibited much less electrical hysteresis compared to the PS-bimetallic sensors with less curve overlap. The low hysteresis in conjunction with high sensitivity and extended linear working range suggests the PO-bimetallic sensors carry a high potential for precise measurements and high-resolution monitoring of large dynamic ranges. Durability of the PO-bimetallic sensors was also confirmed by running the pre-conditioned samples through repetitions of 0-100% strain for 1000 cycles at 6.54 mm s^{-1} and observing a stable profile (**Figure 2.7**).

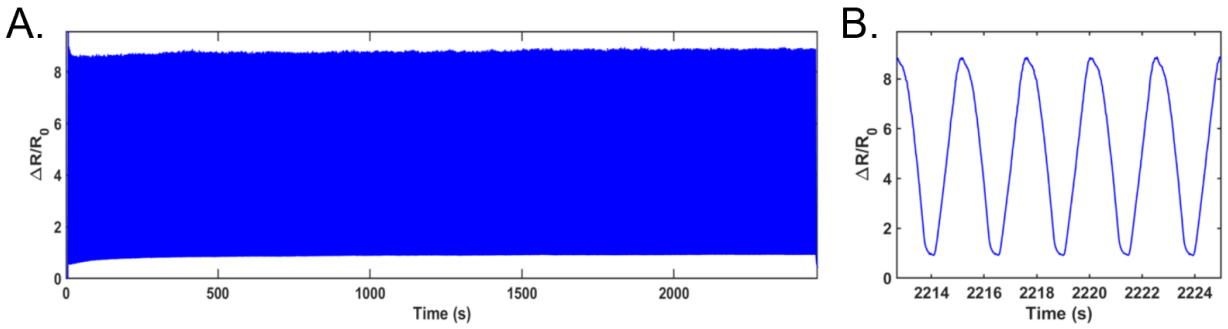

Figure 2.7 Durability of the PS-bimetallic sensors. A) Sensor data from 1000 cycles of 0-150% strain. B) Subset of data showing signal consistency and stability.

Response and latency times were taken using the sensors from the sensitivity test. All sensors were stretched (for 10 cycles) from 0% to 50% at 12 mm s^{-1} and held for 10 sec before returning to 0% and relaxed for 30 sec. For PO-bimetallic sensors, the 10 cycles were repeated for 0-100%, 0-120%, and 0-150% strain levels. Sensor response was defined as the average elapsed time for the electrical signal to surpass three standard deviations of the noise after stretching.[47] The average durations for the stretched sensor to reach the 10% threshold of its stable resistance value at each strain level was taken as the stretched latency; the relaxed latency was similarly defined for the relaxation portion of each cycle.

Figure 2.8 shows profile of the sensor response and latency while **Table 2.1** lists the average response and latency times for each sensor type at different strain levels. Average values and standard error of the mean were calculated using the mean values (across ten cycles) of 6 samples. The response times of the PO-bimetallic (26 ± 5 ms) and PS-bimetallic (27 ± 5 ms) sensors were comparable, suggesting that shrinking on PO instead of PS does not impact the responsiveness of the strain sensors. The responsiveness was also comparable across different strain levels, suggesting the sensors can monitor a large range of strain without significantly changing the signal-to-noise ratio. Less variation in latency was measured in the PO-bimetallic sensors, supporting previous observation of less hysteresis. The stretched latency was found to decrease with increasing strain levels whereas the relaxed latency increased with increasing strain. At higher strain levels, the sensors were closer to the end of their linear range of in-plane elongation or approaching the non-linear response range where a higher frequency of fracture nucleation and elongation occurs.

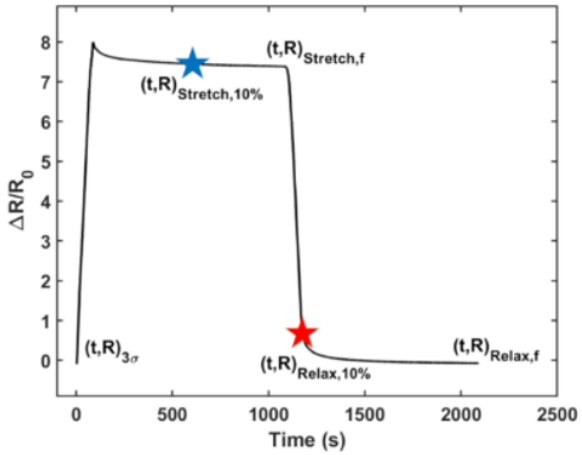

Figure 2.8 Response latency curve of a PO-bimetallic sensor. The sensor was stretched to 100% strain with a 10 sec hold, and then relaxed to 0% strain with a 30 sec hold. The blue and red stars indicate the 10% thresholds used to calculate the stretched and relaxed latencies in Table 2.1.

Table 2.1 Response and latency times at various strain levels.

Sensor Type	Strain	Response Time	Stretched Latency	Relaxed Latency
PO-bimetallic	50%	56 ± 1 s	6.5 ± 0.1 s	0.64 ± 0.03 s
	100%	25 ± 0.4 s	5.3 ± 0.1 s	0.74 ± 0.02 s
	120%	23 ± 1 s	5.2 ± 0.1 s	0.85 ± 0.02 s
	150%	24 ± 0.4 s	5.4 ± 0.2 s	1.0 ± 0.02 s
PS-bimetallic	50%	27 ± 0.3 s	5.4 ± 0.5 s	0.72 ± 0.04 s

2.5.3 Gold stretchable wires

PO wires made from 25 nm Au (PO-Au) and the same design geometry as the PO-bimetallic sensors were explored as a stretchable wire with high conductivity and low sensitivity to strain. **Figure 2.9** shows the STF and sensitivity data of the PO-Au wires. Using Au as the functional material lowered the nominal resistance to as low as 10 Ω. Compared to the PO-bimetallic sensors, the PO-Au wires exhibited greater stretchability and lower sensitivity. The greater stretchability of the PO-Au wires could be explained by the more malleable Au compared to the more brittle platinum. While the sensitivity was not significantly lower than that of the PO-bimetallic sensors, the low nominal resistance of the PO-Au qualified the wires as a stretchable and highly conductive

alternative to commodity rigid wires. Notably, these wires outperformed the PS-Au wires reported from previous work on wrinkled thin film electronics.[28]

2.6 Summary

The stretchability and sensitivity of strain sensors were simultaneously improved by utilizing the PO shrinkage platform. The additional shrinkage of PO-based sensors increased both the dynamic range and the sensitivity of wrinkled thin film sensors by two-fold compared to prior published work, overcoming the sensitivity-stretchability trade-off of traditional strain sensors.[9] With high stretchability, improved sensitivity, and low hysteresis, the PO-bimetallic sensors are equipped to handle motion sensing and control over joints and other high-strain areas of the body. High resolution motion sensing benefits applications that require fine motor control such as finger prosthetics, remote surgeries, VR maneuvers, and motion rehabilitation, adding to the arsenal of conformal wearable technologies available for human physiological monitoring. More information on the fabrication of PO-based electronics can be found under U.S. Patent No. 10,780,688 B2 titled "Highly Wrinkled Metal Thin Films Using Lift-off Layers."

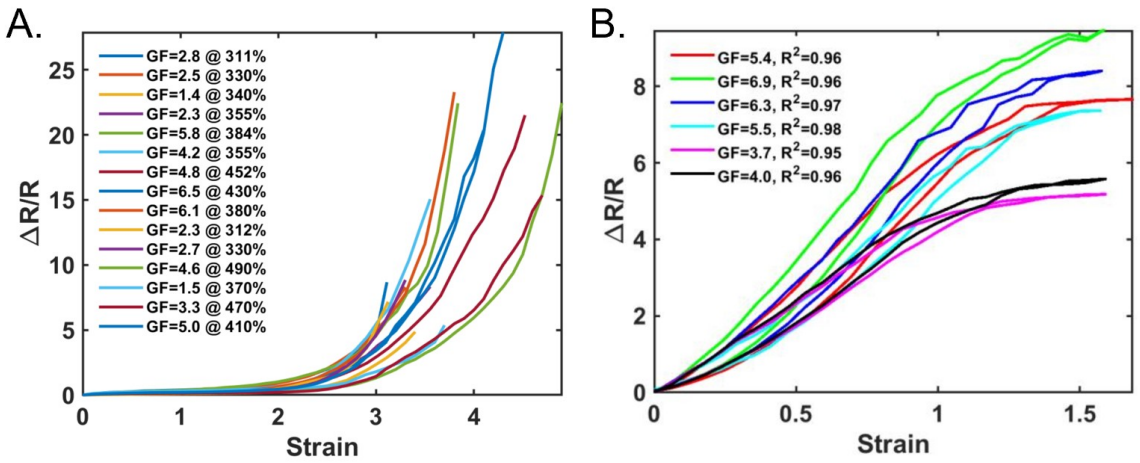

Figure 2.9 Dynamic range and sensitivity of PO-Au wires. A) STF curves. B) Cyclic sensitivity curves straining the sensors from 0-150%.

CHAPTER 3: Application of stretchable sensors for rehabilitation of joint motion

3.1 Introduction

The standard healthy knee joint has a approximate range of motion (ROM) of 0 to 150º, where 0º equates to full leg extension and 150º is the fully bent or flexed position.[48] After sustaining trauma or undergoing operative intervention, human joints such as the knee exhibit limited bending range due to inflammatory swelling or loss of normal mobility. When swollen, the knee can lock at 60º and significantly limit the mobility necessary to engage in daily activities. Impaired mobility limits the alignment of the joint, increasing the likelihood of developing pathological conditions such as arthritis, excess adduction, and load-induced cartilage failure.[49] Further, a reduction of healthy exercising habits, particularly in patients with pre-existing chronic diseases, can impede the quality of life and jeopardize patient outcomes. For these reasons, timely and effective intervention is necessary to prevent permanent pathological joint damage.

To regain general mobility, a healthy knee should experience a minimum bending range of 0 to 120º. Physical therapy is instrumental at restoring early joint motion to aid strengthening the surrounding muscle and tissues. The timely restoration of joint motion is crucial for minimizing the post-traumatic formation of scar tissue that lead to knee laxity and consequential motion loss.[50,51] To ensure optimal post-traumatic outcomes, it is essential for the patient to comply with the prescribed therapy and to perform the exercise with feedback and oversight. In practice, this oversight is limited; the patient is largely expected to comply with the prescribed at-home therapies outside the clinic and loses expert feedback on exercise performance.

Current systems for physical therapy and joint rehabilitation predominantly apply analog measurements to assess joint mobility. This includes universal handheld goniometers in clinical

practice and plain radiographs for medical and research diagnostics.[52] The measurements are taken at incremental appointments and are subjective to the user, patient anatomy, and reported compliance. Consequentially, there is a lack of real-time feedback on progress for both the patient and clinician. The patient must perform their at-home exercises by memory and the clinician is unable to verify patient compliance as a assessment of therapeutic efficacy.

The digitization of rehabilitation markers has risen to meet the demands of more real-time feedback and traceable therapeutic progress. In particular, digital electrogoniometers in the form of various on-the-market stretch sensors have been effective at assessing the dynamic knee ROM in adults.[52] But these stretch sensors share a similar drawback: bulkiness. Their rigid, large profiles require excessive use of adhesives and bandages to secure onto the knee, adding user discomfort and problematic constraints to natural movement. For effective and less intrusive monitoring of joint motion, there is a need for conformal and low-profile stretch sensors that can track high-resolution changes in joint angle with real-time feedback capabilities.

This chapter adapts the shrink-induced strain sensors for applications that require large yet sensitive feedback of human motion, specifically over joint regions. Proof-of-concept motion capture was demonstrated on the finger joint, where the form factor and conformal nature of the sensors were also utilized. The scope was then extended to the knee joint. In a pilot study of healthy adults, the strain sensor was compared to commercially available semi-static and dynamic measures of joint motion. Data was used to generate models for sensor calibration and ROMs in healthy adult knees.

3.2 Demonstration of motion capture on the finger joint

The PO-bimetallic sensors from Chapter 2 were used to capture high-resolution joint motion and withstand the high strain. Specifically, the sensor was mounted onto the index finger to measure joint angles of the proximal interphalangeal (PIP) joint. Prior to mounting over the joint, wires were fixed onto the sensor pads via custom copper clamps. Using an anchor setup, the sensor was positioned between the PIP and knuckle joints (**Figure 3.1A**). The anchor comprised of an FDA-approved double-sided skin adhesive on a non-stretchable but flexible thin substrate. The distal anchor was positioned between the distal interphalangeal (DIP) and PIP joints while the proximal anchor was placed between the PIP and knuckle joints. Next, a flexible non-stretching substrate was connected to the sensor via S-shaped hoops and then positioned over the PIP joint. This setup absorbed the bending strain from finger flexion and decoupled the finger bend from the strain of finger flexion, allowing the sensor to only measure planar displacement. Using an ISOM-certified finger goniometer (Blue Jay) with 5° incremental tick marks for verification, the finger was flexed and extended from 0-90-0° at 5° (±1°for human error) increments.

Ten cycles of flexion and extension were recorded and normalized with each increment lasting for 5 seconds. The maximum observed linear displacement was 113%. Each of the 5-second periods were averaged and plotted against their respective joint angle value.

Data was analyzed and plotted using MATLAB software (MathWorks, R2018a). Upon analysis, the sensor was found to exhibit high signal-to-noise ratio with clear differentiation between each 5° incremental step (**Figure 3.1B**) and was found to respond linearly and precisely to changing PIP joint angles. Notably, the resolution was significantly better than predecessor reporting no less than 15° incremental resolution.[29,31,33] The PO-bimetallic sensors showed great potential as a high-resolution feedback monitor for motion control. It exhibited high sensitivity

and linear responsiveness to strain, and its small footprint made it suitable for sites with limited real estate. With its slim and unobtrusive form factor, low-cost manufacturing, and high-resolution sensing, the PO-bimetallic demonstrated utility for the rehabilitation of fine joint motion.

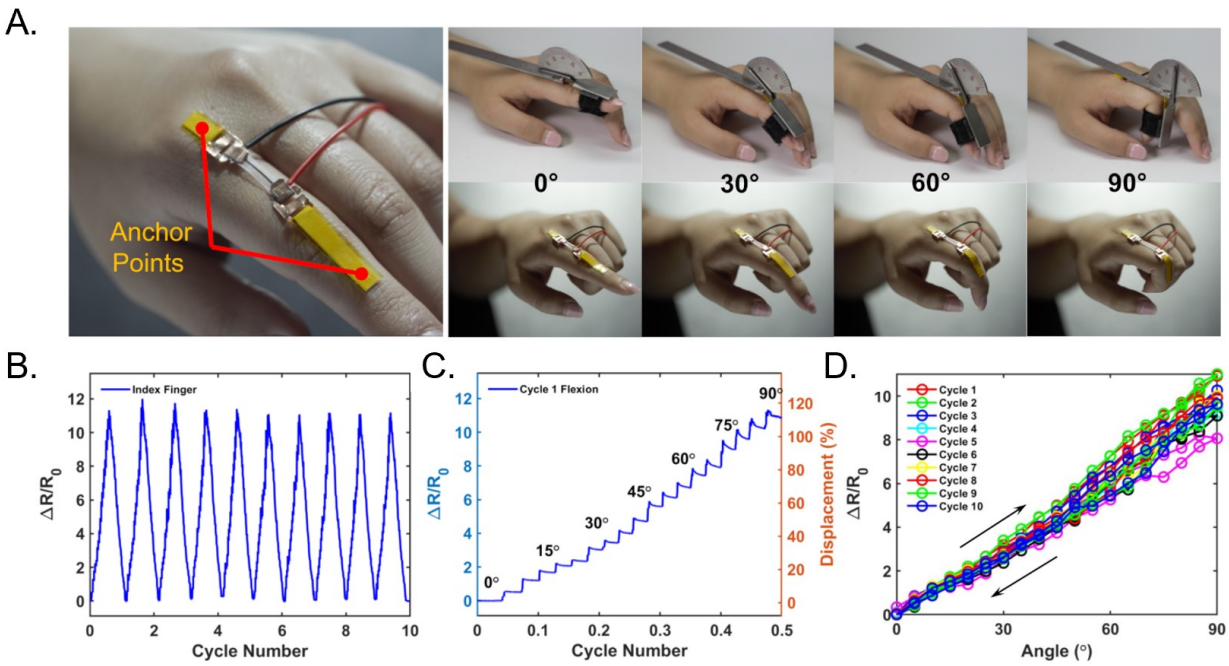

Figure 3.1 Finger joint measurements using PO-bimetallic sensor. A) Distal and proximal anchor setup with the PO-bimetallic sensor positioned between the PIP and knuckle joints. PIP joint angles are verified using a finger goniometer. B) Semi-static signal acquisition of the sensor stretching from 0-90° at 5° increments. Increasing flexion of the finger causes the sensor to stretch planarly. C) Subset of data showing the joint angle increases linearly with sensor displacement and resistance changes. D) Averaged incremental data plotted against the respective joint angle demonstrates cycle precision and sensor compatibility for motion sensing and control.

3.3 Motion capture and model of healthy knee joint mobility

3.3.1 Semi-static motion for sensor calibration

A pilot study was initiated to investigate the use of wearable sensor for digitizing knee joint flexion and extension. PS-bimetallic sensors were used for the knee measurements due to their larger footprint and coverage over the straining joint. The sensors were encapsulated with Ecoflex 00-30 for added durability.[53] Prior to standardized testing with the sensors, a procedure was devised to test and optimize the sensor placement around the knee joint. The field research at a physical therapy clinic (Mariners Physical Therapy, Costa Mesa, CA) revealed that most postoperative patients possess scar tissue spanning the medial line from above to below the knee. This presented an initial challenge to the project because the medial line of any joint produces the most linear strain profile, but the presence less-elastic scar tissue would pathologically change the strain profile of the skin along the medial line. Thus, medial placement was not ideal. Given the pilot scope of healthy subjects, the medial sensor placement was kept for simplified comparison across all subjects. To compensate, a second sensor placed elsewhere was introduced to investigate optimal placement away from the medial line. The placement was as follows: (1) on the anterior knee below/distal to the patella (henceforth known as Sensor 1), and (2) a wild-card placement (Sensor 2). **Figure 3.2A** provides visualization of the various sensor placements while **Table 3.1** lists the sensor placement on each subject.

A semi-static testing procedure was used to investigate the spatial and temporal efficacy of various sensor placements (**Figure 3.2B**). This type of testing incorporated the manual calibration of leg positions using a goniometer, adding measurement accuracy. Prior to testing, each subject's knee was evaluated using a 360-degree ISOM goniometer (Prestige Medical, 12-in) to confirm their ability to bend from 0° (full extension) to 120° (full flexion). Next, the subject was positioned

in a sitting position (hip joint is ~100°) on a flat surface. Using the goniometer, the knee was flexed at 5° increments from 0° to 120°. At each increment, a marker was placed on the surface to identify the corresponding foot placement. During this process, the ankle was kept at 90°. After all markers were placed and verified for accuracy using the goniometer, optimal locations for the strain sensors were determined. Sensor 1 was placed on the medial line below the patella and parallel to the leg. Sensor 2 was placed: at the lateral side of the knee with the sensor parallel to the leg (P2); at the lateral side of the knee with the sensor perpendicular to the leg (also P2); the medial quadricep muscle group (P3); the anterior quadricep muscle group (P4); or the lateral quadricep muscle group (P5). The placement and orientation of Sensor 2 was determined by drawing a mesh grid (3 mm dot spacing) and identifying the location and axis of the greatest planar strain. Once the locations were identified, the sensors were adhered via FDA-approved stretchable skin adhesives (MBK). For Subject 4 onwards, the skin area was pre-treated with a thin coating of tincture of benzoin (Torbot) to aid sensor adhesion and prevent the delamination observed from Subject 3.

At the start of recording, each subject began at full knee extension. Using the foot markers as guides, the knee was flexed at 30° increments until full flexion was achieved (i.e. 0°, 30°, 60°, 90°, and 120°), causing the sensor to lengthen and increase in electrical resistance (**Figure 3.2B**). Then, the knee was incrementally extended back to 0°. Each incremental position was held for 5 sec. Digital time markers (via a wired trigger button) were placed at the beginning and end of each 5 sec period. Once 10 cycles of flexion and extension were collected, the test sequence was repeated from 60°-->120°-->60° at 5° increments. Voltage data from the sensors were passed through a Wheatstone circuit and collected using a data acquisition board (National Instruments, DAQ 6003). Digital time marker data were passed through a voltage divider and collected using the DAQ board. Both data types were collected with a sampling frequency of 100 Hz.

Sensor data were converted to resistance values using SignalExpress software (National Instruments). Digital marker data were processed in MATLAB software (MathWorks) to display 5V when the trigger button was pressed and 0V when depressed. Using the digital time markers, the sensor resistance data were sectioned into the 5 sec incremental periods and the cycle (#1-10) in which the period took place. Each 5 sec period was averaged, and resistance values were normalized in independent cycles.

The flexion and extension cycles were largely comparable in terms of profile and magnitude increase in sensor signal. All placements expressed an increase in electrical resistance in response to increasing strain and bending at the knee. Sensor 1 data from all six subjects exhibit relatively linear profiles throughout the entire tested range (**Figure 3.3A**). For Sensor 2, parallel placement at the lateral side of the knee was determined to be undesirable; the sensor at this location was susceptible to curvilinear straining that caused it to prematurely lift off in Subject 3. To correct for this curvature, Sensor 2 was positioned perpendicular to the leg at the same location for Subject 4, but this resulted in the strain spreading over two axes instead of one and subsequent dampening of the potential signal. Prior to Subject 5 testing, an alternate FDA-approved skin adhesive was tested. This alternate adhesive, made of stretchable and breathable polyurethane, was found to handle large amounts of strain when coupled with the tacky tincture of benzoin. While brainstorming other placement locations around the knee, it was observed that the region of quadricep muscle linking to the patella tendon visually stretched during knee flexion. Thus, this placement was tested. In Subject 5, Sensor 2 data show excellent change in strain, but the electrical resistance was exponentially increasing after 90°. The cause of this effect was determined to be the strain sensor reaching its electrical dysconnectivity after reused testing on multiple subjects. In response, fresh sensors were used on Subject 6, resulting in more linear data, and indicating that

future strain sensors should be reevaluated for quality prior to entering another round of subject testing. In Subject 7, the anterior and lateral quadricep muscle groups (P4 and P5, respectively) were tested due to their active role in stabilizing the knee against excess adduction.

Figure 3.3B compiles the data from all testing locations except the patella. The P1 patella location produced the most linear data (as expected), whereas the P4 anterior quad and P5 lateral quad locations produced the greatest changes in incremental sensor readings. Due to the high incidence of post-operative scar tissue along the patellar line (disqualifying P1), the P4 and P5 locations were determined to be the best locations for digital readouts. **Figure 3.4** plots the detailed data from Subject 7 at 30º and 5º increments. This semi-static data was later used as a calibration model for dynamic motion measurements (next section).

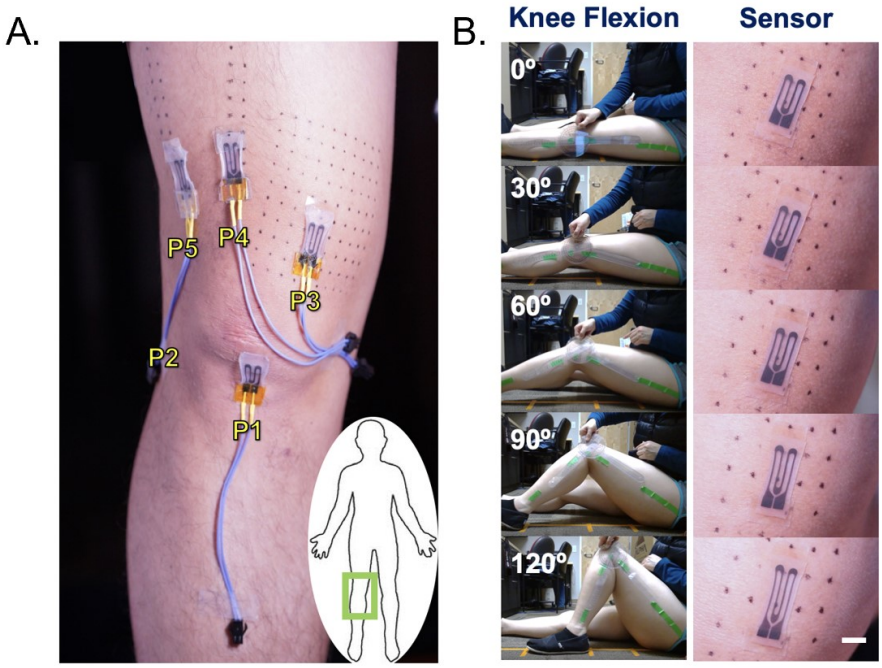

Figure 3.2 Semi-static knee joint measurements. A) Visualization of sensor placement. Sensor 1 was placed below the patella (P1) or medial quadricep (P4). Sensor 2 was placed on the lateral side of the knee (P2) or over various quadricep muscle groups (P3, P4, P5). A mesh was pre-drawn to orient Sensor 2 along the axis of the most linear strain. B-C) Semi-static data collected at 30º increments from Sensors 1 and 2, respectively, with indicated knee placement and dynamic sensor elongation.

Table 3.1 List of subjects for semi-static testing

Subject ID	Age	Gender	Height	Sensor 1 Placement	Sensor 2 Placement
1	26	M	182 cm	Below Patella	--
2	27	F	166 cm	Below Patella	--
3	28	F	157 cm	Below Patella	Lateral Knee (sensor parallel) *
4	21	F	156 cm	Below Patella	Lateral Knee (sensor perpendicular)
5	26	M	175 cm	Below Patella	Medial Quadricep
6	23	F	165 cm	Below Patella	Medial Quadricep
7	23	M	180 cm	Anterior Quadricep	Lateral Quadricep

* Data was not analyzed due to sensor delamination during testing.

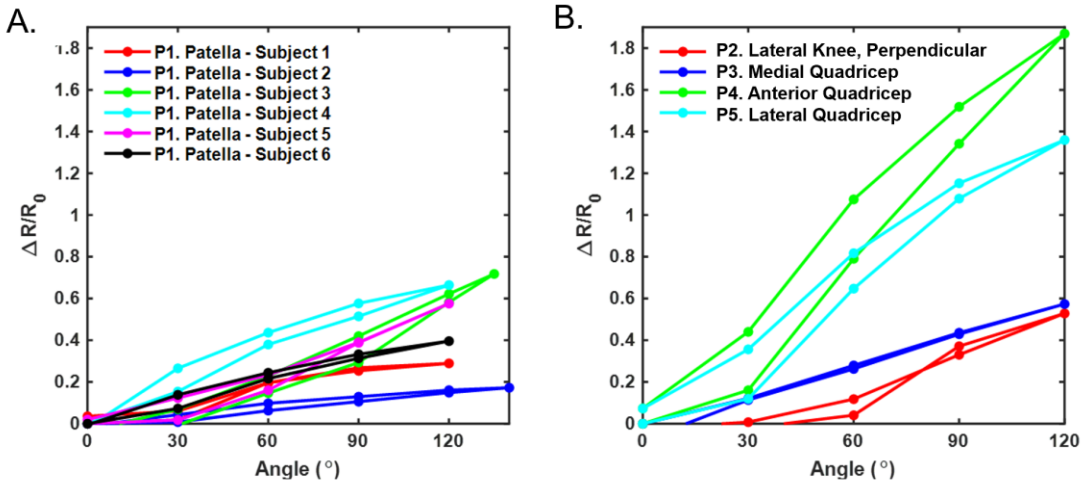

Figure 3.3 Semi-static cyclic data of six subjects recorded from the strain sensors. A) Sensor 1 data from the anterior knee. B) Sensor 2 data from various placements around the knee.

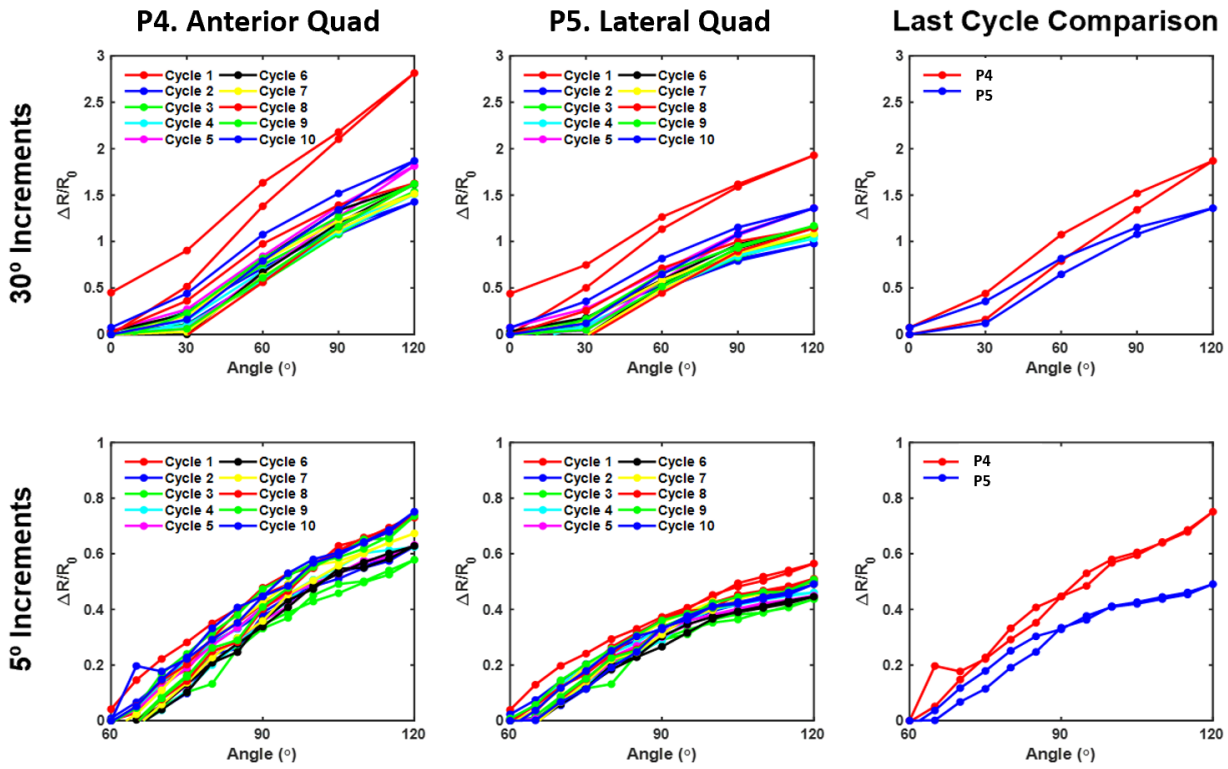

Figure 3.4 Comprehensive set of sensor data taken from Subject 7. Top row: Data taken from 0-120º at 30º increments. Bottom row: Data taken from 60-120º at 5º increments.

3.3.2 Dynamic motion captured on motorized rehabilitative tool

The continuous passive motion (CPM) machine (Kinetec Spectra) is an FDA-approved Class II motorized device for knee joint rehabilitation. It is typically prescribed to passively engage the post-operative knee to expedite recovery and reduce the stiffness of local scar tissue.[54] The machine flexes and extends the injured leg without requiring muscle activation. The speed, ROM, and run cycles of the machine can be tailored to individual rehabilitative needs. During a programmed run, the machine displays the changing joint angle. With the sensors recording from the knee, the continuous sensor readings can be correlated with the dynamic CPM joint readings.

Prior to mounting the sensors, the subject was instructed to lay supine on the floor with the left leg secured on the CPM machine. The leg bolster of the CPM machine was adjusted to fit the length of the subject's tibia and femur bones. After prepping the P4 and P5 skin areas with sterile

isopropanol wipes, mesh grids with 8 mm dot spacings were drawn onto the fully extended knee of the secured leg. The CPM machine was programmed to flex the knee from 0-120º at a linear velocity of 0.5 cm/s for 13 cycles. While running the machine, the mesh grids were observed for dot separation distance and their relevant strain axes. The sensors used for these experiments were approximately 16 cm long and linearly responded up to 30% strain. For this reason, the ideal sensor locations were regions of the mesh grid that underwent 30% uniaxial strain at full knee flexion. **Table 3.2** lists the subjects of the CPM experiments.

Once the placement locations were identified, the sensors were adhered onto the skin. A combination of FDA-cleared double-sided skin adhesives (MBK), kinesiology tape (KT tape), and Transpore tape (3M) secured the sensors onto the skin pretreated with tincture of benzoin. On average, the sensor on the P4 anterior quadricep location was placed approximately 5 cm above the patella and exhibited cleanly uniaxial strain. The sensor on the P5 lateral quadricep location was approximately 4 cm lateral to the P4 sensor and angled 30º away from the centerline of the knee. For each subject, 13 CPM cycles of sensor data were collected on the data acquisition unit at a sampling frequency of 20 Hz. Manual time markers were incrementally flagged on the sensor data for every 5º angle change displayed on the CPM machine.

To prepare the data for analysis, a low pass filter designed in MATLAB screened out high frequency artifacts above 0.005 Hz. The peaks and troughs corresponding to the maximum flexion (120º) and extension (0º) angles, respectively, were digitally identified. Due to the constant linear velocity of the CPM machine, the angular velocity decreased as the knee achieved full flexion and increased while approaching full extension, causing the peaks to appear flattened and the troughs tapered. The CPM machine was paused at 5º increments to measure the elapsed distance of the foot (a total of 53 cm for full flexion). The elapsed distance was matched to the sensor data by

multiplying the runtime with the machine's constant linear speed of 0.5 cm/s. This allowed the interpolation of the CPM angle data to be correlated with the sensor data. **Figure 3.5** shows the sensor's electrical resistance plotted against runtime and interpolated CPM angle. In **Figure 3.5D-E**, the normalized resistance (y-axis) was calculated by dividing the change in sensor resistance (measured minus initial) by the baseline value of the dataset. For each subject, the mean normalized resistance and standard deviation of all cycles was calculated at 5º increments and then plotted against its respective angle measurement.

Table 3.2 List of subjects for continuous passive motion testing

Subject ID	Age	Gender	Height	Sensor 1 Placement	Sensor 2 Placement
1	23	M	180 cm	Anterior Quadricep	Lateral Quadricep
2	23	F	165 cm	Anterior Quadricep	Lateral Quadricep
3	26	M	171 cm	Anterior Quadricep	Lateral Quadricep
4	27	F	171 cm	Anterior Quadricep	Lateral Quadricep
5	27	M	182 cm	Anterior Quadricep	Lateral Quadricep
6	20	F	160 cm	Anterior Quadricep	Lateral Quadricep

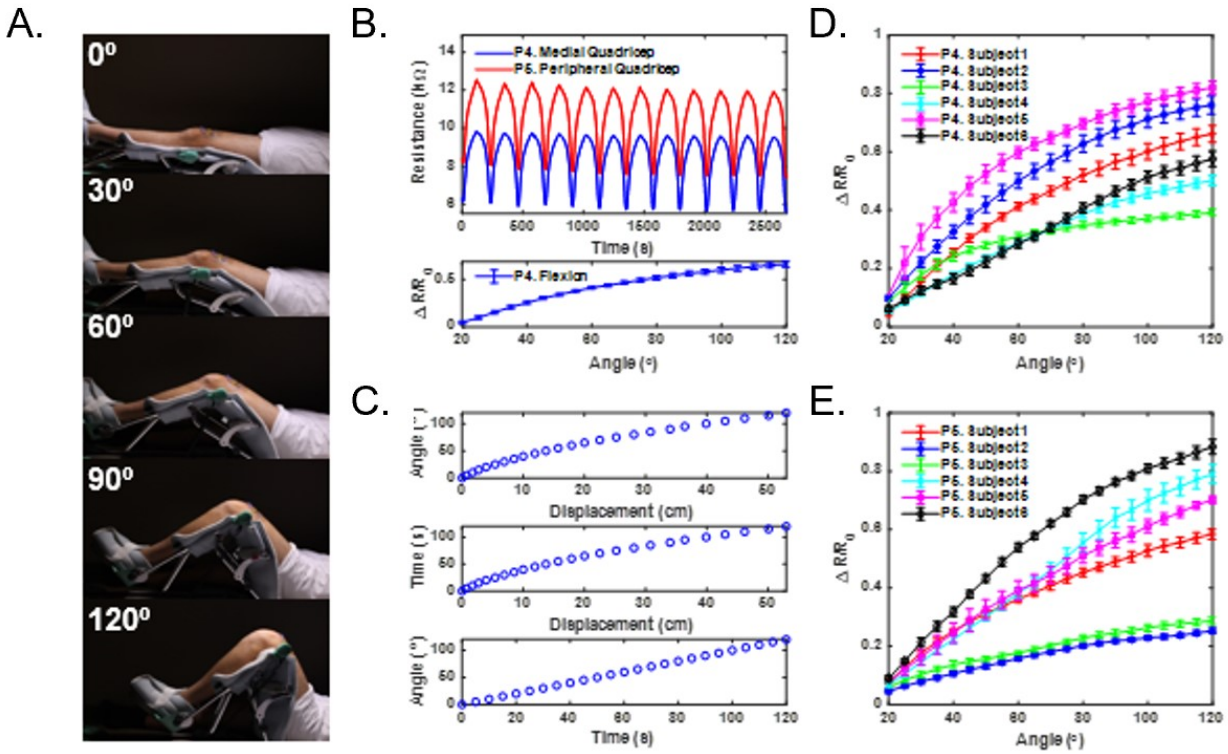

Figure 3.5 Dynamic knee joint measurements. A) Visualization of continuous knee flexion from 0-120º on the CPM machine. B) Top: Data collected from the P4 and P5 sensors exhibit uniform baselines and profiles over multiple CPM cycles. Bottom: Mean flexion data of all P4 cycles with standard deviation calculated every 5º from 20-120º. The first two cycles are excluded and used to condition the mounted sensor. C) Correlation of the sensor data to the knee joint angle via time markers. The distance of the sensor displacement is plotted against the displayed CPM angle readings. D) Mean flexion data from the P4 sensor. E) Mean flexion data from the P5 sensor.

To determine the resolution of the sensor, a one-way ANOVA test was performed on the last 10 cycles (flexion component only) of sensor data from all subjects. (The initial cycles were dedicated to sensor conditioning, and the data was excluded from the statistical analyses.) The flexion cycles, each taken from 0-120º, were broken down into 25 data segments of 5º length (i.e. 0-5º, 5-10º, …, 115-120º). All segments corresponding to the same 5º length were placed in one group (i.e. the 0-5º group contained 10 cycle segments x 6 subjects = 60 segments). Each group was compared against its adjacent groups to determine statistical significance via multiple comparison ANOVA results. If two adjacent groups were statistically significant, then 5º

resolution could be determined. If the groups were not significant, then they were combined to repeat the analysis with 10º length segments and determine if 10º resolution was achieved.

Except for Subject 3, the ANOVA tests determined that the P4 sensor exhibited 10º resolution in the 20-90º flexion range. The P5 sensor exhibited a minimum resolution of 10º in the 10-90º range. Subject 1 data was found to achieve 5º resolution in the 10-110º range. Subject 3 data did not achieve the low resolution observed from the other subject datasets. This was likely attributed to the use of fatigued sensors (used more than three times).

To test the reproducibility of the sensor data, a model fit was generated from the flexion data of each subject. Resistance values at 1º increments were extracted from the flexion cycles to create an experimental dataset consisting of experimental (CPM) joint angles. The incremental value of each cycle was compared to the corresponding values of the other cycles, generating a 3rd degree polynomial fit equation. Due to the changing angular velocity, the first twenty degrees (0-20º) of each cycle exhibited a different profile from the latter portion of the cycle (20-120º). For this reason, a two-model fit was generated—one model for the first twenty degrees, and a second model for the remaining segment of the cycles. For both models, the independent variable was the sensor resistance value whereas the dependent variable was calculated joint angle.

Next, the resistance values from the experimental dataset were inputted into the two-model fit to generate a theoretical dataset containing the calculated joint angles. For each subject, the calculated angles were compared to the CPM experimental angles. The Lin's concordance correlation analysis was performed on both two model fits.[55] The mean value of the two models was designated as the correlation coefficient of each subject. **Figure 3.6** lists the concordance correlation coefficients of each subject. All subject datasets comparing the experimental CPM angles and calculated model-fit angles showed excellent correlation with R values greater than

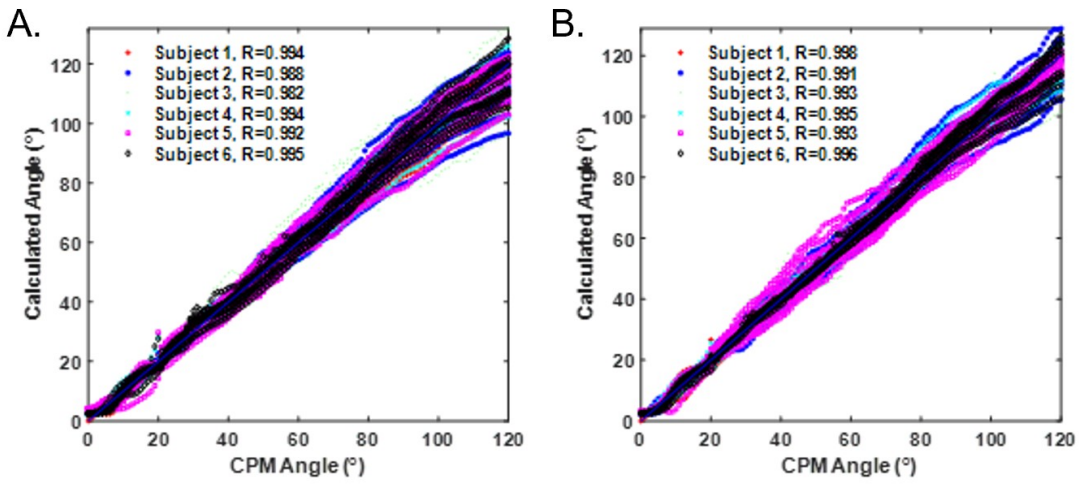

Figure 3.6 Correlation of the calculated angles versus the CPM angles. Concordance correlation coefficients are shown for the A) P4 sensor datasets and the B) P5 sensor dataset.

0.98. The strength of the correlation coefficients demonstrated the high correlation between the sensor data and CPM angle data, as well as the reproducibility of the sensor data for repeated cycles of flexion.

3.4 Wireless joint motion capture

Previously, the joint motion capture experiments used wire setups for conceptual and testing purposes. Having shown that the stretch sensors could record high resolution data with excellent correlation to joint angle, the next step was to incorporate wireless sensing capabilities. A battery-powered Bluetooth unit was connected to the sensors placed at the P4 and P5 locations (see **Figure 3.7A**). The subject was secured onto the CPM machine and underwent six cycles of flexion and extension to condition the sensors. After conditioning, the subject transitioned to exercise performed at the local recreation center. (Only the P5 sensor remained; the P4 sensor was removed due to low-battery concerns of the corresponding Bluetooth unit.) Five squat exercises were performed (**Figure 3.7B**) before transitioning to the treadmill. The treadmill was set to three

speeds, sequentially: 0.8 mph, 2 mph, and 5 mph (**Figure 3.7C**). At each speed setting, the subject jogged for two minutes. Data was transmitted and logged real-time to wireless tablet device.

Upon analysis, the squatting motion caused the stretch sensor to elongate and the resistance value to increase; its peak value corresponded to the fully lowered squat position. Recovery from the squat position enabled the sensor to return to its baseline length and resistance value. For jogging, faster treadmill speed corresponded to increasing frequencies of flexion. The jogging data exhibited two peak types: a primary peak from achieving full flexion, and a secondary peak when the heel struck the treadmill surface. The observed secondary peak was previously reported in human gait analysis and was attributed to the transition from the leg stance phase to the swing phase.[56] The amplitude of the secondary peak represented the impact force registered on the sensor. Overall, the wireless motion capture experiment was successful, and the data includes signal features that could be useful for gait analysis.

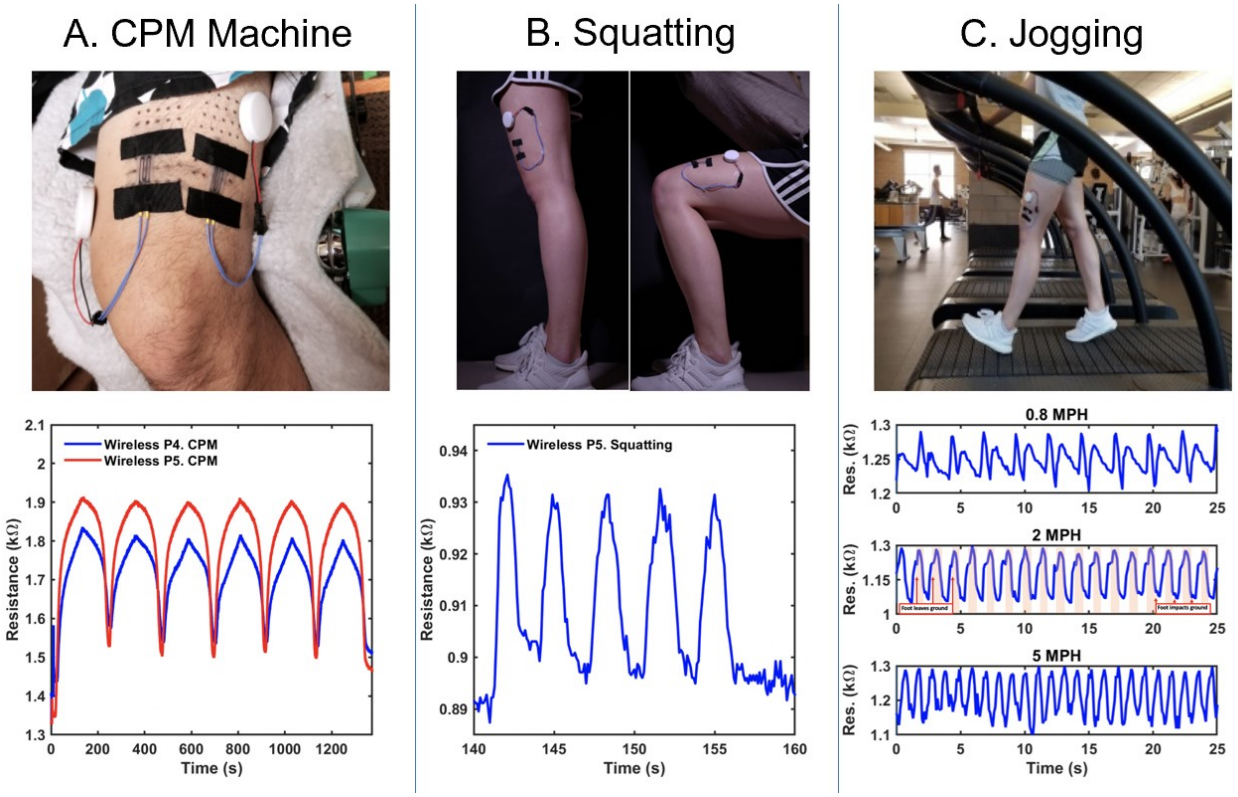

Figure 3.7 Wireless joint motion capture data. Continuous data was taken during A) CPM machine cycling, B) squatting, and C) jogging on the treadmill at various speeds. The P4 and P5 locations were tested on the CPM machine whereas only the P5 sensor was mounted for the squatting and jogging sessions.

3.5 Summary

The wearable stretch sensors demonstrated high-resolution motion capture of the finger and knee joints. Joint angle data collected from the sensors were compared to their industry counterparts, namely the universal goniometer and the CPM machine. The PO-bimetallic sensors exhibited linear responses to finger flexion, low signal hysteresis, and excellent correlation to the finger goniometer angle values. In a pilot study, the PS-bimetallic sensors were applied to the more complex knee joint, where strategic mapping enabled optimal sensor placement for signal reproducibility. Sensor attachment for high-strain applications was improved with the addition of skin-safe double-sided adhesives used in conjunction with coatings of tincture of benzoin. Wireless

monitoring of essential activities like walking and jogging was achieved, and it revealed joint motion data containing features relevant for human gait analysis.

The traditionally low cadence of cumbersome analog goniometer measurements in physical therapy clinics have largely hindered the effectiveness of progress monitoring and patient feedback. CPM machines, due to the lower accuracy of some models, have been unsuitable for standalone operation without secondary, verifiable measurements.[57] The sensors were able to provide real-time digital joint angle measurements after calibrating with a universal goniometer, providing a complementary method of knee flexion analysis for CPM-based therapies. In summary, the stretch sensors were found to be compatible with high-strain applications and add utility as a digital motion monitor for physical rehabilitation needs.

CHAPTER 4: Application of wearable monitors for assessing human physiological health

4.1 Introduction

Physiological monitoring is a major component of managing personal health, sports performance, emotional wellness, and disease management.[58–60] Wearable technologies enable portable and ambulatory monitoring of human vital signs during daily activities and in clinical environments. Emphasis is placed on designing devices with the desired characteristics of comfort, unobtrusiveness, extended wearability, remote usage, and continuous real-time feedback. These features can be found in both consumer and medical-grade devices ranging from the Fitbit activity monitor to the TempTraq temperature patches.[5,61]

Many commercially available monitors measure physiological parameters such as ECG, heart rate, blood pressure, temperature, and blood oxygen saturation.[3,61,62] These monitors predominantly rely on short-tern or discrete measurements as a representative view of overall health. However, discrete "snapshot" measurements can miss dynamic markers that are more indicative of wellness and health.[13] Continuous monitors, particularly for blood pressure, are bulky or require invasive procedures that limit their application for daily monitoring needs.[63,64] There remains an unmet need for continuous and non-invasive wearable technologies for more comprehensive monitoring of physiological vital signs. A system of different monitors that continuously and comprehensively collect multifaceted physiological parameters can provide more clinically significant feedback on patient health.

Conformal soft electronics for continuous monitoring of respiration or blood pressure were previously developed and tested in healthy subjects. Chu *et al.*'s respiration monitor was found to accurately measure respiration rate and volume when compared to a spirometer.[14] Kim *et al.*'s

continuous blood pressure monitor recorded beat-to-beat blood pressure and was validated against an FDA-cleared continuous blood pressure finger cuff (Edwards ClearSight).[13] These physiological monitors have the potential to help individuals that greatly benefit from continuous vitals monitoring. Importantly, they can facilitate the management of chronic diseases and help identify individuals with heighted risks of health problems.

This chapter details the ongoing human subject studies that validate the usage of the conformal soft sensors as clinically relevant physiological monitors. Various pilot studies explore the application of the sensors on healthy and pathologically abnormal subjects. The studies seek to answer whether continuous monitoring motifs can be used for early detection or management of conditions and diseases prevalent in the community.

4.2 Cardiovascular disease

4.2.1 Motivation

Cardiovascular disease (CVD) is the leading cause of deaths in the U.S.[65] Out of the various types of CVD, a major concern is congestive heart failure (CHF). CHF is an end-stage chronic disease with no cure—the heart inadequately maintains blood circulation, resulting in renal complications and other organ dysfunctions.[66] Over 5.8 million people in the U.S. and 23 million people worldwide live with CHF.[67] More than half of those who develop CHF die within 5 years of diagnosis.[68] Complications of CHF is the leading cause of hospitalizations in the U.S. and a major public health issue.[69] In 2015, CHF was responsible for $24 billion in healthcare costs, and the costs are expected to double in the next 15 years.[68] CHF is the only cardiac disease increasing in prevalence.[66]

The leading risk factors of CHF include hypertension, diabetes, and prior incidents of myocardial infarctions (MI).[70] Studies have found that 27% of MI survivors are diagnosed with CHF within 30 days after hospital discharge, and more than one-third will develop CHF in 7-8 years after an MI.[67,71] By monitoring MI patients for early symptoms of CHF, complications, hospitalizations, and deaths can be prevented.[72]

CHF monitoring falls under two categories: 1) tracking onset of symptoms for the purposes of early detection, and 2) monitoring symptoms to manage diagnosed CHF. Due to the progressive severity of CHF, it is advantageous to track disease onset during its early stages. The American Heart Association (AHA) lists early warning signs including increased heart rate, shortness of breath (dyspnea), and fluid retention (edema and weight gain).[72] The presentation of symptoms follows the order of physiological dysfunction, namely: cardiac, pulmonary, and renal conditions. More than 25% of infarcted patients wait ≥ 6 hours after initial symptom onset before seeking medical attention.[73] Delayed medical intervention subsequently advances symptom severity and increases hospitalization time, deaths, and total healthcare costs.[66] CHF disease management is time-sensitive. Early detection and treatment is critical for preventing rapid disease onset and improving mortality rates.[74]

Traditional detection and diagnostic techniques consist of imaging modalities that are not practical for frequent or at-home monitoring needs.[66] Portable devices can monitor body temperature, blood pressure, and thoracic impedance, but they require implantation and primarily service patients with other existing implants like pacemakers.[63] Non-invasive monitoring technologies exist on the market, but they largely focus on late-stage symptoms like fluid retention.[6,75,76] There remains an unmet need to continuously and non-invasively monitor at-risk patients for the earliest signs of CHF. A comprehensive system of physiological monitors can also

benefit patients diagnosed with CHF by providing real-time passive feedback of the effects of prescribed medical and therapeutic interventions. By studying the effects uniquely experienced by each patient, the clinician can more accurately tailor the prescribed therapies for effective disease management.

4.2.2 Pilot study on congestive heart failure

Chu *et al.*'s respiration sensors and Kim *et al.*'s blood pressure sensors were previously tested on young healthy volunteers and showed good measurement correlation against commercialized medical devices.[53,77] This pilot study on CHF, funded by the UC Irvine Institute for Clinical and Translational Science (ICTS), investigated whether the sensors could compare with FDA-approved medical devices across healthy and diagnosed individuals. Additionally, the conformal wearable electronics were evaluated for their potential to detect respiratory and hemodynamic parameters that could differentiate CHF patients from health subjects.

The study was conducted under the approved UCI IRB HS #2016-2924 with a partial HIPAA waiver. Subject-identifiable information was viewed by authorized personnel for recruitment purposes only. The subjects were recruited at the UCI institutional main and UCI Health campuses. Criteria for inclusion was broadly defined for subjects who could give consent and follow instructions in the English language. For CHF subjects, recruited patients had a left ventricular ejection fraction (LVEF) of less than 40%. For healthy controls, subjects were screened for unremarkable medical histories and no discernible risk of developing CVD. The healthy subjects were also recruited with age- and gender-matching intentions for comparison with the CHF subject group. **Table 4.1** lists the subjects enrolled in the study to-date.

Subjects were instructed to avoid exercise and limit consumption of caffeinated drinks and meals three hours prior to the testing time. Informed consent on the study scope, its potential risks, and non-identifiable media recordings were obtained via signature prior to the start of the test. Subjects diagnosed with CHF were additionally instructed to fill out the EQ-5D and KCCQ Questionnaires to assess their present quality of life (QOL) and mobility limitations. All subjects were compensated at the end of each session.

Testing was conducted using a system of non-invasive, passive sensors and monitors (see **Figure 4.1**). Respiration was monitored using conformal strain sensors and a commercially available spirometer (BIOPAC, Inc.). Beat-to-beat (B2B) blood pressure was monitored using conformal capacitive-based pressure (CAP) sensors and a commercially available continuous blood monitor (Edwards ClearSight, CS). Electrocardiography (ECG, BIOPAC, Inc.) and accelerometers (MC10 BioStampRC) complemented the system to provide more real-time physiological information and identify motion artifacts. FDA-approved medical adhesives were used to adhere the sensors onto the skin.

Subjects were positioned in the supine position. Three pre-test and post-test reference blood pressures each were taken using a brachial blood pressure cuff (Omron HEM-7600T-Z). The CAP sensor was placed over the radial artery on the wrist. An arterial line (A-line) support split (AliMed) was used to immobilize the same wrist. It also projected the radial artery for enhanced signal collection. The accelerometer was adhered to the dorsal side of the hand on the same arm. The CS finger cuff was attached to the middle finger of the other arm. Disposable ECG electrodes were adhered to the torso in the Lead II configuration.

All sensors and monitors were simultaneously activated to sync the recorded data. For the first three minutes of the test session, subjects were instructed to breathe into the spirometer to

correlate the change in resistance of the respiration strain sensor and the breath volume captured by the spirometer. During this period, subjects sequentially performed three respiration maneuvers: shallow, normal, and deep breathing. Each level was performed for one minute. A nose clip was used to block airflow through the nose during the maneuvers. After three minutes, the spirometer and nose clip were removed, and the subject was instructed to breath normally for the remainder of the ~20-minute session. At various time points, the subjects were asked to perform deep or normal breathing maneuvers.

ECG (voltage), spirometer (liters per second), and strain sensor (voltage) data were recorded using the AcqKnowledge data acquisition software (BIOPAC Systems, Inc) with a sampling frequency of 2 kHz. The pressure sensor (capacitance) data was acquired using an LCR meter (Agilent Technologies) with a sampling frequency of ~50 Hz. ClearSight B2B blood pressure data with a sampling frequency of 200 Hz was obtained from its EV1000 clinical platform database. The accelerometer (G-force) and gyroscope (degrees per second) data was obtained using the MC10 mobile application and cloud storage database. All datasets were processed and analyzed using MATLAB software (MathWorks).

Table 4.1 Subject data of CHF pilot study

Subject ID	Gender	Age	Subject Group	NYHA* Classification	LVEF**, Report Date
1	M	54	CHF	II	15% on 12/2018
2	F	42	CHF	II	56% on 04/2019***
3	M	54	CHF	II	29% on 03/2019
4	F	68	CHF	II	17% on 01/2019
5	M	67	CHF	II	34% on 07/2019
6	F	43	Healthy	N/A	N/A
7	F	54	Healthy	N/A	N/A
8	M	61	Healthy	N/A	N/A
9	M	48	Healthy	N/A	N/A
10	M	70	Healthy	N/A	N/A

* New York Heart Association functional classification of heart failure on a scale of I-IV
** Left ventricular ejection fraction
*** Result from one motion after test date. Prior result was 25-30% on 07/2018

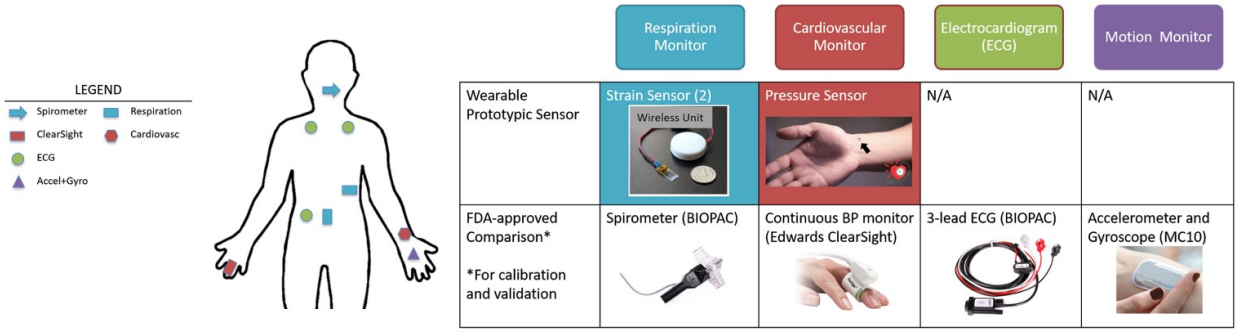

Figure 4.1 Sensing components used in the CHF study

4.2.3 Hemodynamic parameters

Many hemodynamic parameters of continuous, beat-to-beat (B2B) pulsatile waveform data have been extracted and studied for their clinical significance. Heart rate variability (HRV) is calculated by measuring the peak interval times between sequential pulsatile waves, and has been used to assess cardiovascular autonomic regulation.[78] A larger variance is correlated with healthy cardiac function. Blood pressure variability (BPV), calculated as the transient variance of systolic

and diastolic blood pressure values, has been linked to CVD risk and outcomes.[79,80] The variance of double product (DP)—the product of heart rate (bpm) and systolic blood pressure (mmHg)—has been strongly correlated to baroreflex activity, which is necessary for regulating against acute blood pressure changes.[81]

For B2B blood pressure, the CAP sensor and CS system showed robust agreement with R2 = 0.765 for systolic blood pressure (SBP) and R2 = 0.902 for diastolic blood pressure (DBP) in healthy subjects [9]. However, for CHF subjects, the correlation was not as robust. A possible explanation was the presence of implanted cardioverter-defibrillators (ICDs) in certain CHF patients.

HRV was calculated by measuring the R-to-R time intervals that correspond to the sequential zeniths of ventricular contractions.[82] The presence of an ICD obscured the PQRST waveforms of ECG data and was observed in three of the CHF patients with ICDs (**Figure 4.2**). Compared to normal ECG data, the R-peaks of these subjects were difficult to discern. HRV calculated using the pressure sensor data was not reported for Subject 2 since the data contained excess motion artifacts. Excluding Subject 2, the HRV values corresponding to the CAP and CS datasets were not significantly different. The p-values of the deep and normal breathing maneuvers were 0.652 and 0.269, respectively. The average HRV values were 15.03±4.54 for CHF-CAP, 16.5±5.45 CHF-CS, 52.58±17.39 for Healthy-CAP, and 51.23±17.06 for Healthy-CS.HRV in healthy subjects was found to be 3x greater than the variation in CHF subjects. Both the healthy and CHF subjects individually exhibited a large HRV difference across deep and normal breathing maneuvers. To compare this difference between healthy and CHF subjects, Poincaré plots were used visualize the HRV of two representative age- and gender- matched subjects of the same age but in different health condition (**Figure 4.3**). A greater spread, corresponding to greater HRV,

was found in the healthy subject compared to the CHF subject; this result matched literature expectations.[83]

BPV was calculated as the standard deviation of the continuous, B2B systolic and diastolic blood pressure values. Prior to calculation, each subject dataset was manually analyzed to exclude any heart palpitations. Excluding Subject 2, the healthy subject group on average exhibited greater systolic BPV (5.74) compared to the averaged CHF subject group (3.85). When plotted against LVEF, the systolic BPV (SBPV) was found to be positively correlated with improved cardiac output (**Figure 4.4**).

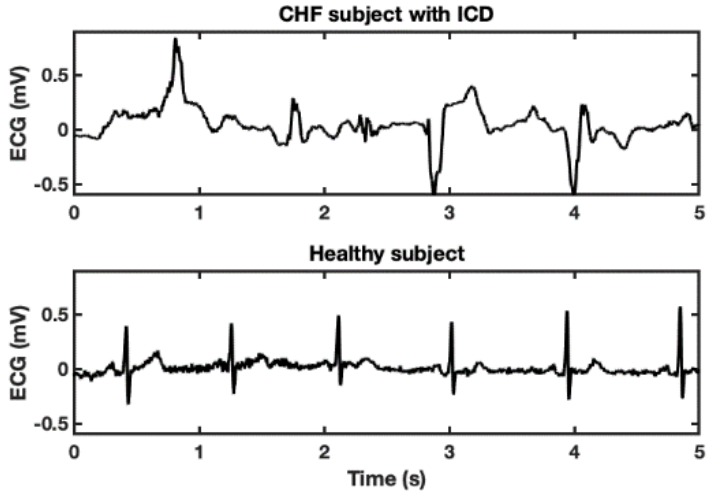

Figure 4.2 Comparison of ECG recording with and without ICD

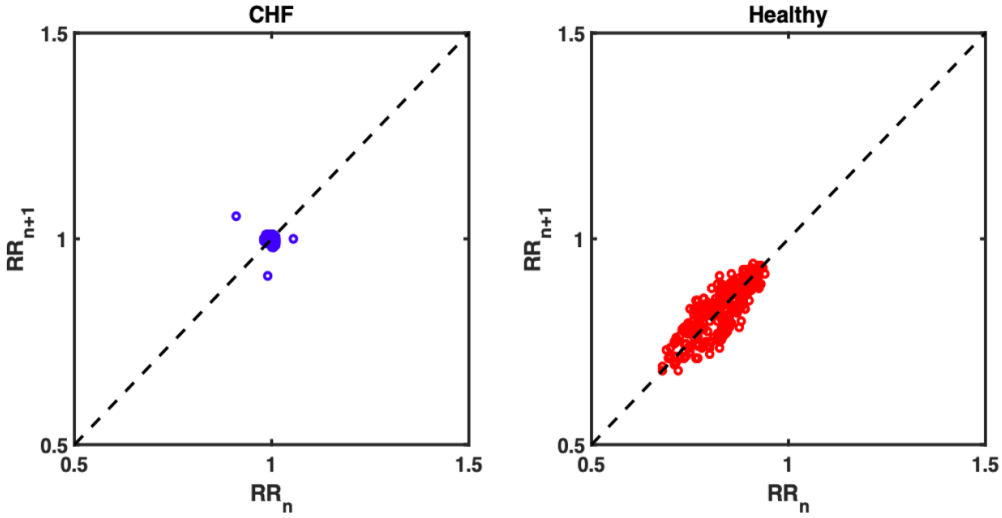

Figure 4.3 Poincaré plot of HRV in CHF and healthy subjects

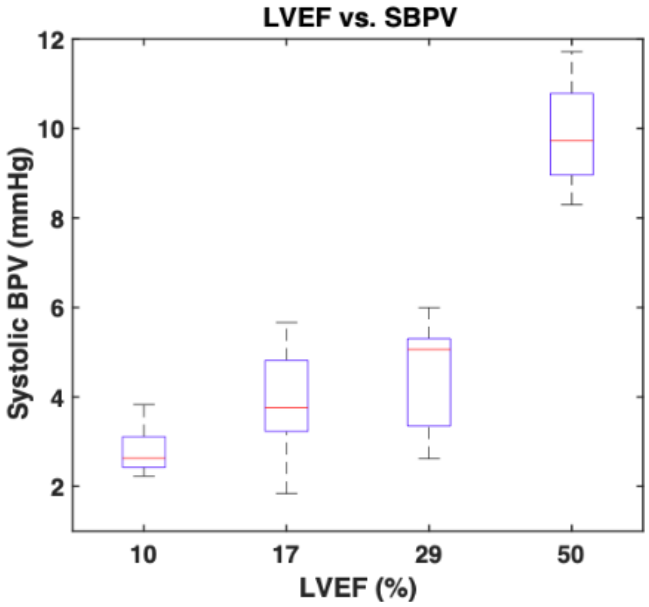

Figure 4.4 Relationship between SBPV and LVEF

Transient DP variation of CHF and healthy subjects were found to produce visibly different patterns. More DP variation was found in healthy subjects, suggesting that DP is also a potential differentiator of the CHF versus health subject groups.

4.2.4 Respiration parameters

Disordered breathing is the most common co-morbidity affecting 50-80-% of patients with advanced CHF.[84] Pulmonary and thoracic edema (fluid build-up) cause CHF patients to transition from healthy diaphragmatic breathing to more laborious abdominal breathing.[85] Abdomen-dominant breathers activate their abdominal muscles earlier than the diaphragm, creating a phase lag between abdominal and thoracic expansion during inhalation. Sleep apnea, or the temporary cessation of breathing, is commonly observed in individuals with abdominal breathing tendencies. Obstructive sleep apnea (OSA) is caused by physical upper airway obstruction. Central sleep apnea (CSA)—more prevalent in CHF patients—occurs when the central nervous system ceases respiratory muscle activity and airflow. In severe CHF cases, CSA produces abnormal respiration

patterns (Cheyne-Stokes respiration) that are characterized by cycles of progressively faster and deeper breaths, followed by apnea events.[18,86] Daytime observation of Cheyne-Stokes respiration in ambulatory patients has been associated with increased mortality, supporting the clinical need for continuous respiration monitoring in CHF patients.[87]

During Subject 1's test (a CHF subject), the subject accidentally fell asleep. At various time points, the subject's breathing terminated for ~30 secs. These events were captured by the respiration sensors. Upon inspection of the thoracic (rib) respiration data, the events were found to resemble CSA episodes: the breathing became increasingly shallow as depicted by gradual drops in signal amplitude, followed by a period of indiscernible breaths, and finally a large recovery breath (**Figure 4.5**).

Data from the thoracic and abdominal respiration sensors were analyzed for indications of phased breathing. Sections of continuous respiration data taken during normal or deep breaths were run through wavelet convolution analysis to assess the direction (positive values equated to earlier abdominal activation) and magnitude of any present phase lag. The results from Subjects 1-9 are consolidated in **Figure 4.6** with "+" and "o" markers denoting CHF and healthy subjects, respectively. Under normal breathing conditions, only Subject 1 was observed with a large positive phase lag. In comparison, the deep breathing conditions introduced more segregated results. Large positive phase lags were found in Subjects 1, 4, and 5 (all diagnosed with CHF), whereas all the healthy subjects maintained similar normal and deep breathing lag values. Abdomen-dominant breathing patterns surfaced when some CHF subjects switched to breathing deeply and more laboriously, suggesting that thoracic and abdominal respiration patterns could potentially differentiate CHF and health cohorts.

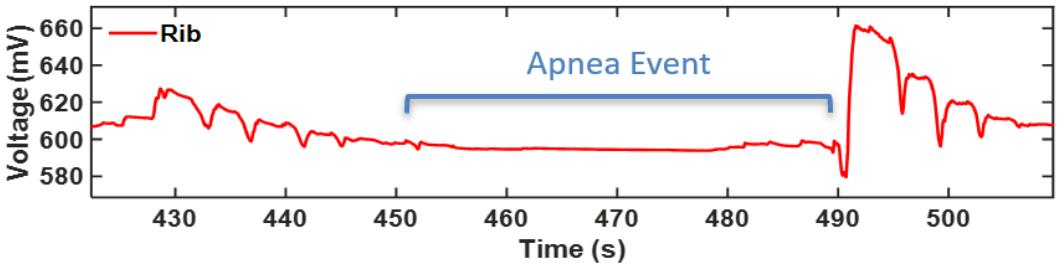

Figure 4.5 Obstructive sleep apnea event detected using the strain sensor

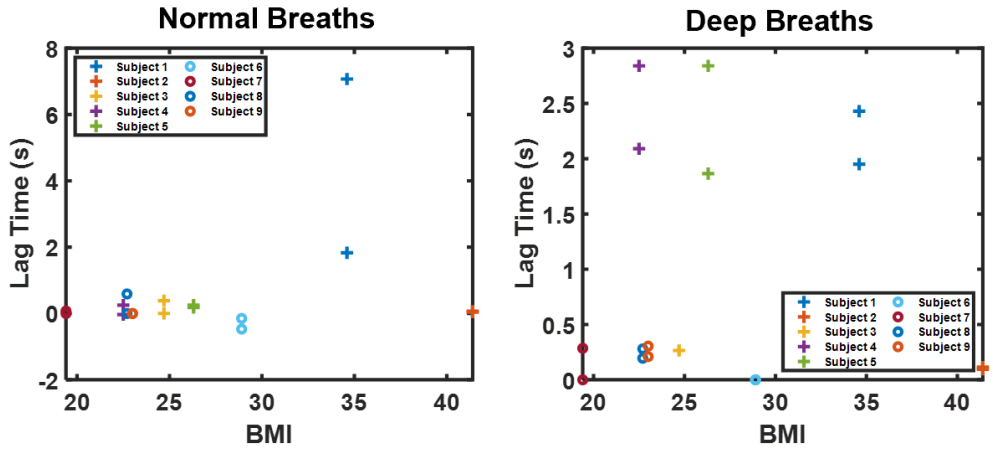

Figure 4.6 Respiratory phase lag between the thoracic and abdominal sensor data. Positive lag times denote earlier abdominal muscle activation and delayed diaphragm activation. The "+" and "o" markers represent CHF and healthy subjects, respectively.

4.2.5 Summary

To summarize, five CHF and five healthy subjects have been tested to-date. Various hemodynamic characteristics were analyzed from the subject datasets including HRV, DP, and BPV. The preliminary data analysis linked lower B2B variance with the presence of CHF, supporting the need for continuous B2B BP monitoring. Variance could be used to distinguish between healthy and CHF sample populations for early detection purposes. The discovery of a positive relationship between LVEP and SBPV from the CAP sensor data potentially associates SBPV with CHF severity and treatment efficacy, adding a positive avenue for disease management. The respiration sensor recorded an observed apnea event and could potentially be used to monitor for daytime ambulatory Cheyne-stokes respiration patterns. The initial success of

the CAP and respiration sensors from monitoring subjects with diagnosed abnormal pathology adds utility to conformal sensors as ambulatory and at-home continuous physiological monitors. Moreover, their complementary form factors and monitoring motifs allows them to form the basis of a system of conformal physiological monitors.

4.3 Early cardiovascular health

4.3.1 Motivation

The prevalence of CVD in the U.S. draws demand for timely assessments of CVD risk. A prominent risk factor of CVD is arterial stiffness. Blood vessels become less elastic with increasing age and the presence of chronic conditions (e.g. diabetes and hypertension) that can erode endothelial tissue and allow atherosclerosis.[88,89] Damaged or stiffer vessels are more likely to calcify and develop blockages, which can cause aneurisms, stroke, and myocardial infarctions.

Endothelial function can be assessed by directly visualizing the dilation of the coronary artery in response to acetylcholine injection, but the method lacks widespread clinical use due to the invasive nature of the method.[90] A non-invasive alternative uses Doppler ultrasonography to visualize flow-mediated dilation (FMD) of the brachial artery.[91] In this technique, the brachial artery is temporarily occluded to stimulate nitric oxide (NO) production from the downstream endothelium. NO instigates vasorelaxation and inhibits constriction factors, enabling the artery to dilate in effort to increase downstream blood flow.[92] The post-occluded artery is compared to its unperturbed size to assess vasodilation, but the measurements are subjective to operator experience.[93]

The EndoPAT, an FDA-cleared non-invasive FMD-based method for assessing endothelial dysfunction, uses plethysmography-based finger cuffs to detect flow changes from the finger.[94]

The brachial artery is occluded for 5 minutes to induce endothelial secretion of NO. The blood flow in the finger after occlusion is compared to the flow prior. The ratio of the flow amplitudes is used to determine the reactive hyperemic response. Large post-flow to pre-flow ratios (index value greater that 1.6) are indicative of normal endothelial function. However, this method can be cost-prohibitive due to its elective procedural status under certain reimbursement schemes.[95]

The reactive hyperemic index is one of several metrics for determining peripheral artery disease (PAD). Another promising parameter of arterial stiffness is the augmentation index (AI). The AI compares the wave of a heartbeat "reflected" from the peripheral arteries to the initial elected wave. A larger difference in peak heights signifies more elastic arteries.[88] But peak analysis necessitates high-resolution pulsative waveforms that contain minute peak-to-peak variances. Arterial wave reflections have been linked to cardiovascular events and the risk of developing CHF.[96] The capability to analyze the small wavelet features will likely strengthen early CVD detection.

4.3.2 Pilot study on endothelial health

The non-invasive continuous blood pressure (CAP sensor) was tested for their potential significance in reactive hyperemic analysis. Subjects were recruited into a medical clinic that performed EndoPAT reactive hyperemic tests. The tests were modified to include simultaneous monitoring with the CAP sensor.

Prior to testing, the subjects were instructed to fast for a minimum of 8 hours. Each subject was placed in a comfortable supine position before taking their pre-test blood pressure with a brachial arm cuff. The systolic blood pressure value was used to determine the brachial occlusion pressure (+30 mmHg). Next, the EndoPAT plethysmography finger cuffs were attached to the

subject following equipment instructions. On the non-dominant arm, the CAP sensor was placed over the radial artery. An accelerometer was placed on the dorsal hand to monitor for motion artifacts. The Edwards ClearSight finger cuff was attached to the middle finger of the dominant arm.

Upon starting the sensor recordings, the subject was instructed to relax and lay still to collect pre-occlusion baseline data. After 5 minutes, an arm cuff was quickly inflated to the specified pressure. Occlusion of the brachial artery lasted 6 minutes and was confirmed by visually observing flatline data. After releasing the occlusion, the post-occlusion blood pressure and flow waveforms were collected for 6 minutes. **Table 4.2** lists the subjects of the reactive hyperemia study.

Table 4.2 Subject data of the reactive hyperemia pilot study

Subject ID	Gender	Age	Height	Subject Group
1	F	42	154 cm	Healthy
2	F	28	166 cm	Healthy

4.3.3 Waveform analysis

On the EndoPAT, Subject 1 (42 y.o. female) registered a healthy reactive hyperemic index (RHI) greater than 2. Initial inspection of the CAP sensor data showed a large post-occlusion signal amplitude that supported the high RHI. (**Figure 4.7**). Upon B2B analysis, the CAP sensor revealed a post-occlusion transient shift in waveform shape (**Figure 4.8A**). Prior the occlusion, three peaks of successively smaller amplitudes were observed in each pulsatile wave. Immediately after the occlusion was lifted, the second peak overtook the first peak in amplitude. The post-occlusion waveform shape took approximately 5 minutes to recover its original pre-occlusion shape.

Subject 2 (28 y.o. female) similarly registered a healthy RHI index on the EndoPAT system. In contrast to Subject 1, the CAP sensor pre-occlusion waveform of Subject 2 had a less

distinguishable second peak (**Figure 4.8B**). Immediately after occlusion, the second peak combined with the first peak to form a broad-looking peak. Within three minutes, the post-occlusion waveform returned to its pre-occlusion shape.

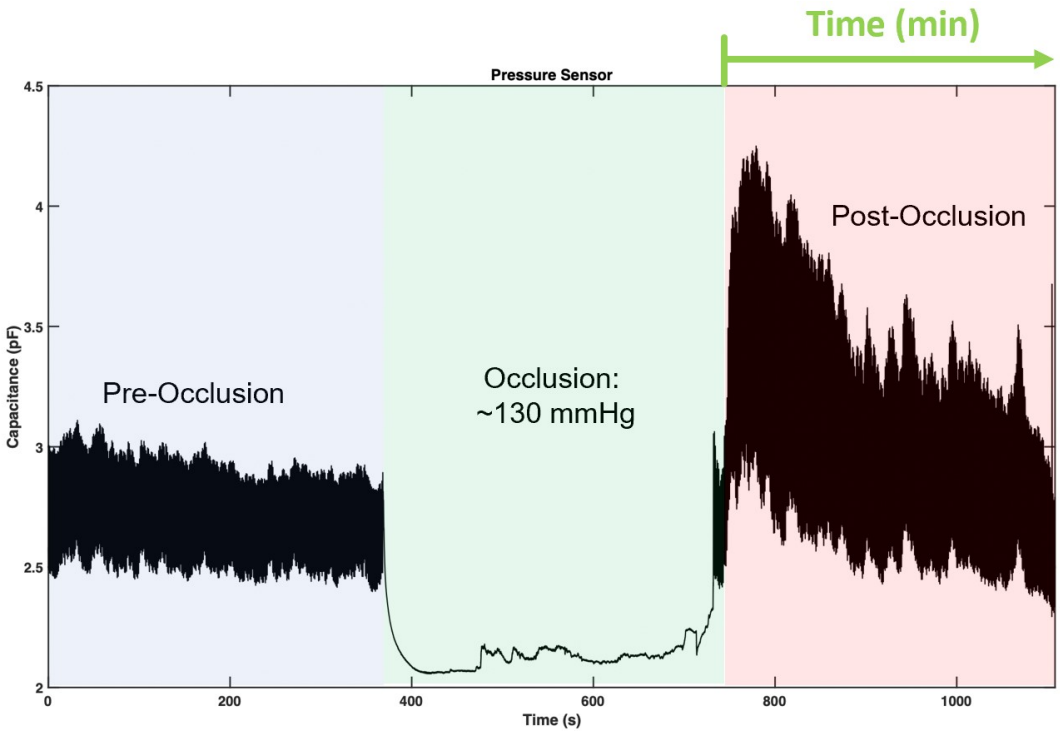

Figure 4.7 Reactive hyperemic response of Subject 1

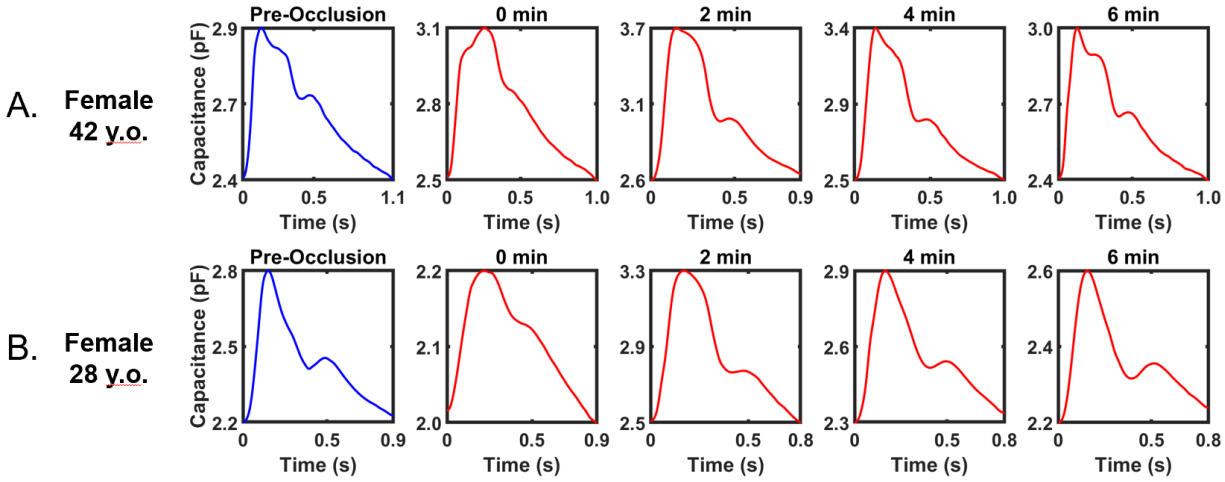

Figure 4.8 Age comparison of waveform shape after brachial occlusion

In radial applanation tonometry, the second peak represents the reflective wave. A prominent second peak has been associated with the reduced elastic compliance of the peripheral arteries.[97] Based on this information, the CAP sensor suggested that Subject 1 was at risk of developing PAD (contrary to her unremarkable medical history).

To further investigate the data, the 1st and 2nd derivative of the CAP sensor data was calculated and plotted in MATLAB (**Figure 4.9**). Comparing the 2nd derivative waveform to the Elgendi's acceleration plethysmogram (APG), Subject 1 was characterized to possess good, but deteriorating blood circulation.[98]

4.4 Summary

Human vitals monitoring has largely been limited to clinical settings due to technological and cost constraints. Existing portable technologies for personal health management can provide basic information like blood pressure and heart rate, but their rigid form factors discourage extended wear, and the discrete measurements lack transient insight on a person's dynamic health. There is still a need for comfortable and continuous collection of physiological data, particularly in the field of cardiovascular disease.

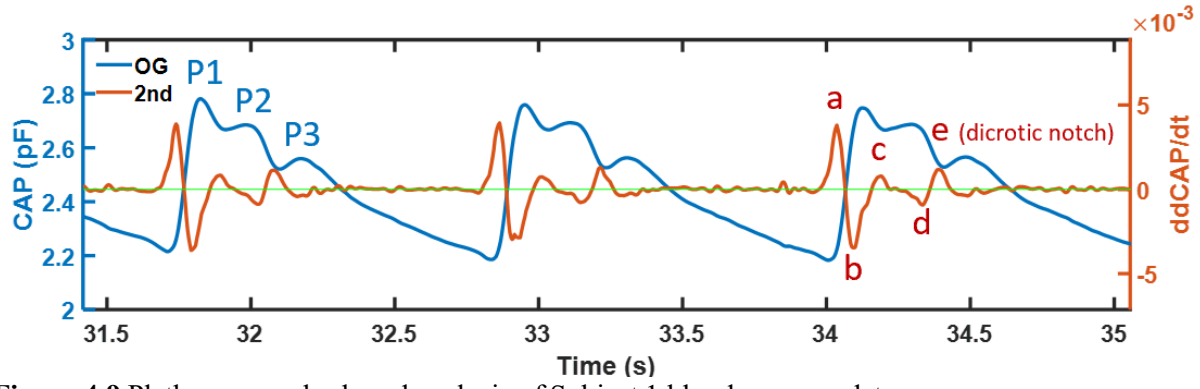

Figure 4.9 Plethysmography-based analysis of Subject 1 blood pressure data

For the first time, the conformal and soft respiration and blood pressure sensors were used to collect continuous and beat-to-beat physiological data from medically impaired subjects. The CHF pilot study aimed to identify digital biomarkers for early detection and management of the chronic disease. Various hemodynamic and respiration parameters emerged as potential indicators of CHF, and the clinical significance of other detected signal features remain to be investigated. Ten subjects have been enrolled to-date. A parallel pilot study on the reactive hyperemic response of the brachial artery explored the efficacy of radial applanation tonometry for assessing arterial stiffness. Features found on the blood pressure waveforms were found to transiently change with vessel size. Through plethysmography-based analysis, the waveforms offered clues to the endothelial health and CVD risk of the subject.

Additionally, the similar form factors of the respiration and blood pressure sensors facilitate their integration into a comprehensive system wearable monitors, providing a more in-depth coverage of personal health and chronic diseases.

CHAPTER 5: Conductive skin ink for highly conformal and wireless electronics

5.1 Introduction

Wearable sensors and electronics have largely emphasized the aspects of conformity, stretchability, and unobtrusive profile for improved wearability and ambulatory considerations.[16,99] They continuously evolve to be increasingly epidermal-like by modulating their thickness and stiffness to maximize moldability to the natural roughness of skin.[7] Yet, the current development stages of such technology coupled with their inherently complex manufacturing processes limit the electronics development to pre-determined configurations and applications.[100–102] The ability to print systems of epidermal electronics on demand remains elusive.

Design manufacturability and overall form factor of the wearable electronics are also constrained by the power consumption and direct communication needs for the capture and transmittance of physiological data over prolonged time periods.[34,103] While individual sensing components may achieve miniaturization and good skin fidelity, in practice the monitoring systems are often tethered to bulky and rigid power sources and discrete data acquisition and communication modules (e.g. Bluetooth). To combat this limitation, many research groups have pursued efforts to develop battery-free and wireless wearable sensors for various applications.[104–110] These emancipated sensors are instead designed to communicate with customized, modular, or off-the-shelf components such as loop antennas and near-field communication (NFC) chips.[111,112] The modular additions of such components require sensors to undergo multi-step processing and interfacing which complicate their manufacturability and scalability. It also constrains the sensors within prefabricated designs.

Another unmet demand of wearable electronics is the availability of conformal "dry" electrodes. Physiological monitors such as electroencephalography (EEG), electrocardiography (ECG), and general electrodermal activity (EDA) necessitate excellent skin contact area for quality signal acquisition.[113] Disposable commercial silver/silver chloride (Ag/AgCl) "wet" electrodes use adhesive hydrogel layers to maintain flush skin contact and act as a salt bridge between the skin and electrode surfaces. However, the hydrogels can dry out, reduce the electrode conductivity, and decay the signal quality over time. For this reason, skin-safe "dry" electrodes are desirable to meet the technical demands of extended monitoring periods. Dry electrodes with lesser skin fidelity have been developed to address this need, but they compensate the skin contact by increasing surface contact area via bulky and obtrusive designs.[114] They also rely on externally applied pressure or tensile forces to add consistency in skin contact.[115–117]

This chapter shifts the focus to other key factors of ubiquitous wearable sensors and electronics: skin compliance, design versatility, and on-demand customization. Manufacturing motifs using conductive inks can meet the demands for excellent skin contact, ease of component interfacing, and fluidic design choice.[118–121] The non-toxic conductive ink described here addresses the desire for dry electrodes, rapid and on-demand sensor manufacture, and wireless and battery-devices.[122]

5.2 Craft glue-based ink formula

5.2.1 Materials choice

Conductive inks made from liquid metal (e.g. gallium-indium) are commonly used for printing flexible electronics, but they are susceptible to undesirable formations of low-conductivity oxide skins and stiffness mismatches with their support substrates that challenge their robustness

for wearable applications.[12,123] Alternatively, conductive inks touted for their skin-safe formulas are comprised of suitable, highly conductive metal precursors [e.g. micro- and nanoparticles (NPs) made from gold (Au), silver (Ag), copper (Cu), and carbon (C)] that are stabilized with non-toxic polymer bases and binders.[101] Of the common metal precursors, carbon-based inks are a cost-effective choice, but they suffer from brittleness once dried and are unsuitable for applications that demand extended skin wear.[10]

Ag is a suitable candidate for broad-spectrum wearable electronics due to its documented non-toxicity, antimicrobial properties, and usage in wound dressings.[124,125] Further, Ag/AgCl is non-polarizable and therefore attractive for EDA and other sweat sensing applications.[115] Conductive inks made from AgNPs or nanowires (NWs) exhibit high electrical conductivity (10^5 $S \cdot m^{-1}$) and can be manufactured into screen-printed wearable sensors and electronics, but nanoscopic particles are undesirable for their potential respiratory and transcutaneous hazards.[126–128] Very small particles such as AgNPs can penetrate the skin barrier and bind with subcutaneous proteins, causing argyria or permanent skin discoloration.[124] In contrast, larger Ag particles (i.e. Ag flakes) are less prone to crossing the skin barrier and can be printed onto the skin.[129,130] Thus, Ag flakes were chosen as the function material for the conductive ink for their conductivity, biocompatibility, and non-hazardous size.

Ag ink found in literature require the use of high concentrations of Ag flakes to achieve sufficient conductivity, use less skin-safe stabilizing polymers, or suffer from low ductility.[127] The ductility of skin-printed electronics is necessary to withstand deformations from general motion and to allow for extended skin wear without risking delamination. As such there is a need for skin-safe conductive inks that possess high conductivity while retaining ductility when dried.

Specifically, ductility sufficient to withstand approximately 30% strain is necessary for physiological applications.[131]

Ag flakes are commercially available in average particle sizes (APS) between 2-10 μm and selective coatings for epoxy or silicone compatibility. At the time of project conceptualization, the 2-5 μm APS silicone-compatible Ag flakes (Inframat Advanced Materials #47MR-71F) were readily available. For this reason, most of the characterization in this chapter was performed on conductive ink made with this type of Ag flakes. A second type of Ag flakes was procured and preliminarily tested in conductive ink formulas: the 2-4 μm APS epoxy-compatible Ag flakes (IAM #47MR-10F).

Various conductive ink formulas exist in literature. Polymer bases commonly chosen for the conductive inks include polyvinylpyrrolidone (PVP) and poly(3,4-ethylenedioxythiophene) polystyrene sulfonate (PEDOT:PSS).[130,132] PEDOT:PSS has gained popularity for its native conductivity, but requires extended preparation, handling, and storage. Instead of using polymers prepared in a laboratory setting, the base material was chosen from commercially and readily available products. Inspired by quick-drying craft glues, the search landed on PVA-based Elmer's Glue-All® multipurpose glue (henceforth referred as PVA glue). Multiple advantages followed this choice, including non-toxicity, shelf-stability, wide availability, and superb affordability.

To prepare the Ag ink, weighed aliquots of PVA glue were thoroughly hand-mixed with Ag flakes in a 1:1 (w/w) or desired ratio. Glycerol was optionally added to the mixed ink to produce a smoother formula (1-5% by weight). The ink could be prepared in advance and ambiently stored in a capped container (e.g. disposable syringe) to resist drying. Ink allotments were re-mixed or discarded after seven days to minimize gravitational settlement and fluctuations in electrical conductivity. A single layer of Ag ink (~90 μm thickness) applied with a spatula or similar tool

was found to dry after 30 minutes in ambient conditions, similar to standalone PVA glue. The drying time was lowered to 5 minutes with the addition of body heat (e.g. from skin application) and convection (e.g. nearby fan). The Ag ink passed a 24-hr skin patch test without eliciting any noticeable irritation.

5.2.2 Conductivity characterization

To determine the electrical conductivity of Ag ink, the following formulas of Ag:PVA glue using silicone-compatible Ag flakes were prepared into flat test strips: 1:2 (w/w), 1:1 (w/w), 1:1 (w/w) with 1% glycerol [1:1(1%)], and 1:1 (w/w) with 5% glycerol [1:1(5%)]. Additionally, a 1:2 (w/w) formula of Ag:PVA glue using the epoxy-compatible Ag flakes was also tested (henceforth referred as 1:2"). Each test strip was 20 mm long and 5 mm. The sample thicknesses were controlled by using stencil masks of different known thicknesses; the thickest samples were made by laminating together multiple layers of stencil material to create thicker masks. Each condition tested six thicknesses ranging from 70-300 μm, each with n=3, for a total of n=18 data points. All test strips were dried overnight to encourage consistent results.

Electrical resistivity (the inverse of conductivity) measurements were taken by probing the resistance across a 5.5 mm length in the middle of each Ag test strip. Resistance measurements with respect to strip thickness were plotted in MATLAB (MathWorks). Using the relationship between thickness and resistance value (**Eq. 2**), a non-linear least square fitting curve was used to calculate the electrical conductivity of each Ag ink formula:

$$\gamma = \frac{1}{R} \times \frac{l}{A} \qquad (2)$$

where γ = electrical conductivity, R = electrical resistance, l = sample length, and A = sample cross-sectional area determined by the width and thickness.

The ductility of each Ag:PVA condition was determined by subjecting 90 μm-thick Ag test strips under strain-to-failure (STF) testing, in which each test strip was strained at a constant rate while resistance changes were continuously logged using a precision LCR meter (Keysight Technologies E4980AL). To control the strain rate, the test strips were loaded onto a motorized linear actuator (Zaber X-NA08A25-E09) with a set nominal gap length of 5.5 mm and linear velocity of 10 μm/sec.

Representative conductivity and STF results (for ease of interpretation) are shown in **Figure 5.1**; the data including 1:2" (w/w) [epoxy-compatible Ag] is listed in **Table 5.1**. Ink conductivity increased with Ag concentration but was found to decrease with the addition of glycerol. Conversely, ductility was observed to decrease with Ag concentration yet improved with the addition of glycerol. The results suggested a general trade-off between resistivity and ductility with increasing Ag concentration. Because of its greater Ag concentration, the 3:2 (w/w) ratio was found to strain less than the 1:1 (w/w) ratio. After straining past 50%, fractures were observed in the 3:2 samples that elongated until mechanical failure, suggesting there was an insufficient makeup of the less-stiff polymer base. Concentrations greater than 1:2 (w/w) were found to strain past the 30% wearability threshold necessary to adequately strain with skin, thus demonstrating the minimum ductility necessary for electronic and sensing applications (e.g. electrodes painted on the forearm or other non-bending areas). As a result, the condition with the highest reported conductivity (1:1, no glycerol) was chosen as the Ag ink formula for application testing and sensor fabrication described in the latter half of this chapter. At this ratio, dried ink samples consisted of 7.1.6% Ag flakes by weight, using 20% less Ag than previously reported.[129] Scanning electron microscopy (SEM, FEI Magellan 400) images, provided in **Figure 5.2**, were taken to visualize the dispersal of the Ag flakes of each ink condition. The Ag ink made with the epoxy-compatible Ag

flakes (1:2" formula) was found to require less conductive material (55% Ag flakes by weight) compared to the Ag inks made with silicone-compatible Ag flakes. At this concentration, it achieved a similar conductivity level as the 1:1 (w/w). The knowledge that PVA glue preferentially mixes with epoxy-compatible functional materials benefits future conductive ink development.

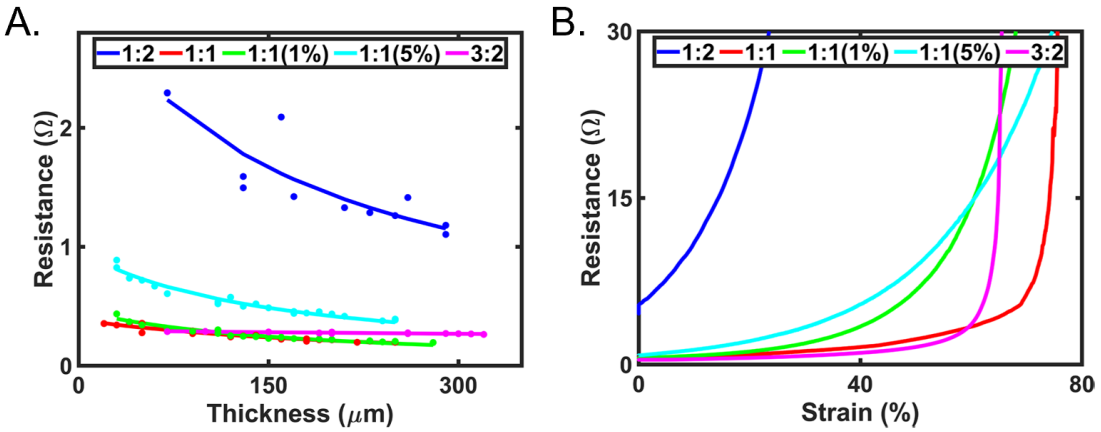

Figure 5.1 Characterization of the conductive Ag ink. A) Electrical resistivity curves. B) Strain-to-failure as a measure of ductility.

Table 5.1 Conductivity and ductility characterization of various Ag ink formulas.

Formula	Conductivity	Strain-to-Failure	Elastic Modulus
1) 1:2 (w/w)	1.7 x 10^3 S·m^{-1}	53.2%	--
2) 1:1 (w/w)	1.2 x 10^4 S·m^{-1}	76.9%	56.5 ± 3.8 MPa
3) 1:1 (w/w) + 1% glycerol	1.4 x 10^4 S·m^{-1}	83.7%	53.1 ± 2.1 MPa
4) 1:1 (w/w) + 5% glycerol	7.7 x 10^3 S·m^{-1}	97.0%	18.9 ± 1.0 MPa
5) 3:2 (w/w)	1.3 x 10^3 S·m^{-1}	68.6%	--
6) 1:2 (w/w) [epoxy-type]	2.0 x 10^4 S·m^{-1}	38.9%	1.24 ± 0.19 MPa

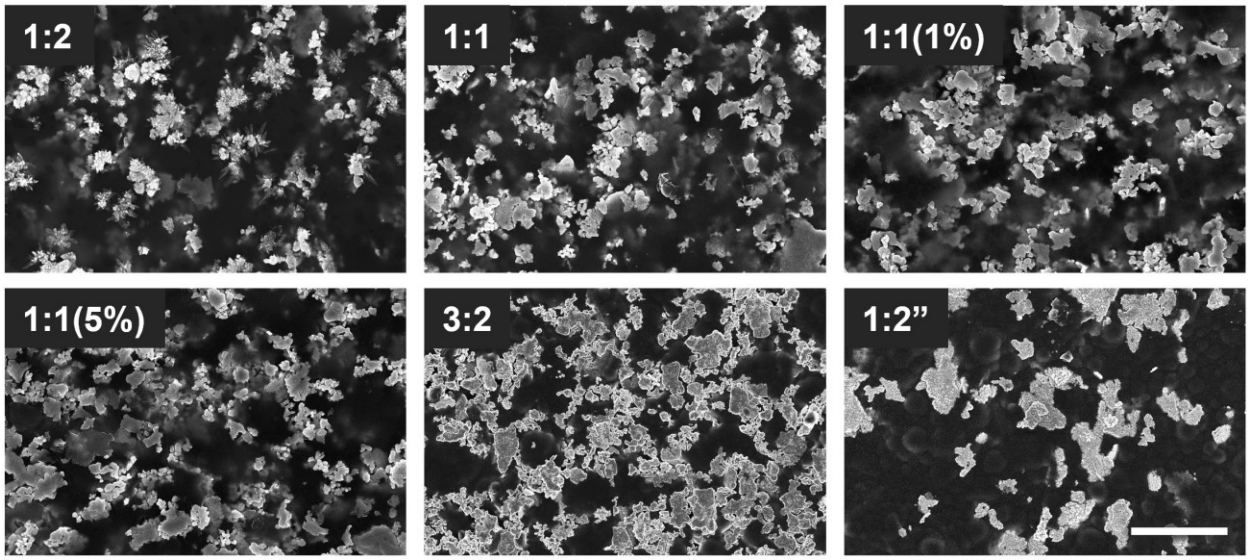

Figure 5.2 SEM images of the various Ag:PVA concentrations. Scale bar is 10 μm.

The Ag ink test strips were further characterized under a dynamic mechanical analyzer (DMA, TA Instruments Q800). The elastic moduli and standard error of the mean (n=3) for the 1:1, 1:1(1%), 1:1(5%), and 1:2” formulas are listed in **Table 5.1**. The elastic moduli of the four tested conditions suggested that the stiffness of the Ag ink films could be tuned by thinning the PVA glue with glycerol. Although the 1:1 condition was stiffer compared to the elasticity of skin (4.6-20 MPa), in practice the ink was painted thin enough to prevent premature delamination.[43] The 1:2” condition remains an excellent candidate for future development of Ag ink formulas.

5.2.3 Direct skin application

In the basic principle of paint application, wet paint is applied onto a surface of reasonable roughness, allowed to flow into the surface features, and then dry with flush contact to the surface. Similarly, the wet Ag ink could first be painted onto textured skin, flow into skin grooves (e.g. fingerprints, wrinkles), and then dry to become a custom-molded, on-demand epidermal electronic. To add design versatility, the direct skin application was coupled with simple, pattern-cut adhesive

stencil masks. The masks were designed using engineering computer-aided design (CAD) software and then rapidly manufactured using a laser cutter. Resolution of the design features were limited by the laser cutter's beam width and heat-affected zone (~200 μm, depending on the laser power and dwell time). Grafix Frisket Film, both the low-tack and high-tack variants, was a choice masking material due to its thinness and low paint seepage. Ideal feature sizes were 1 mm and above to avoid premature mask delamination during the ink application.

Figure 5.3 provides a schematic of the on-skin ink application process plus examples of the tattoo-like Ag ink electronics on the index finger and forearm. First, the desired area was cleaned using water or rubbing alcohol to remove any residual oils and enhance ink adhesion. Next, the adhesive stencil mask was adhered over the prepared area. Using a flat spatula, the Ag ink was painted over the entire design area. After achieving an even coating, the mask was carefully removed, leaving behind the desired Ag ink pattern. Once fully dried, the Ag ink tattoo could be used on-demand. Optionally, medical-grade adhesive or liquid bandage (e.g. Nexcare) could be applied over the dried Ag ink to waterproof the tattoo and add electrical insulation. To remove, the Ag ink tattoo could be washed or rubbed off with some water. Alternately, applying an adhesive tape or bandage and then peeling it off would also (elegantly) remove the tattoo.

Upon removal via adhesive tape, the Ag ink tattoo on the finger was found to have molded the papillary ridges of the fingertip (**Figure 5.3C**). Viewing the tattoo under a 3D laser scanning microscope (Keyence VK-X100) suggested the topography of the tattoo closely matched the skin roughness and that excellent skin contact was achieved.

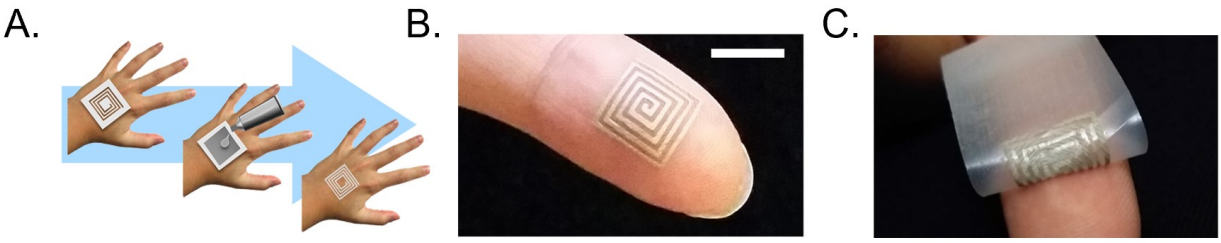

Figure 5.3 Visualization of the conductive Ag ink tattoos. A) Process flow for patterning the Ag ink onto the skin using a disposable adhesive stencil mask. B) Example of an Ag ink tattoo patterned over the fingerprint region of the index finger. Scale bar is 1 cm. C) Removal of the Ag ink tattoo via adhesive tape shows impressions of the papillary ridges.

5.2.4 Temporary tattoos

In addition to on-demand skin application, the Ag ink could be prefabricated to prepare sensors and electronics in advance. Depending on the sensor and application, the Ag ink was patterned onto various support materials including medical-grade polyurethane adhesive bandage (3M Tegaderm®), polydimethylsiloxane (PDMS) membranes, stretchable silicone (Ecoflex 00-30), and temporary tattoo paper (Silhouette of America). The support materials also served as insulating layers for the multi-layer sensors, in which each layer was pre-patterned and allowed to dry before stacking into a single device.

Ag temporary tattoos were fabricated by patterning Ag ink onto inkjet printer-compatible temporary tattoo paper with the help of low-tack adhesive stencils. A double-sided adhesive was laminated over the dried ink following manufacturer instructions. **Figure 5.4** shows examples of Ag ink patterned onto temporary tattoo paper. The tattoo was transferred onto the wrist by dissolving the release layer with a damp cloth.

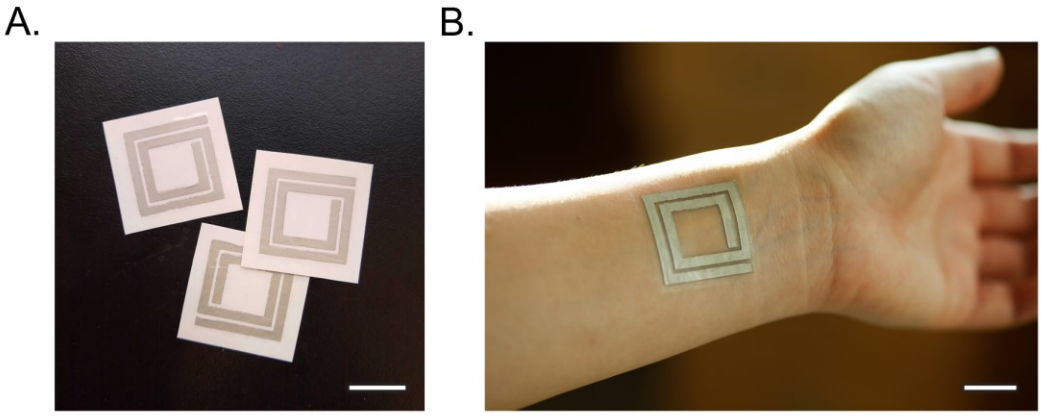

Figure 5.4 Conductive temporary tattoos. A) Ag ink coils are pre-pattered onto temporary tattoo paper. B) Tattoo is transferred onto the skin by applying a damp cloth. Scale bars are 2 cm.

5.3 Paint-on dry electrodes

5.3.1 Electrocardiography

Electrocardiography (ECG) measurements typically necessitate electrodes with excellent conductivity and skin contact. Disposable Ag/AgCl ECG "wet" electrodes have achieved maximal skin contact by utilizing their adhesive hydrogel layers, but the hydrogels dry out and reduce the electrode conductivity over time. Meanwhile, skin-safe "dry" electrodes that rely on externally applied pressure or tensile forces (textiles, adhesive support materials) suffer from inconsistent skin contact.[115–117] Thus, there is a need for dry ECG electrodes can maintain excellent skin contact.

Ag electrodes (2 cm-wide disks) were painted onto the back of the hands (positive, negative) and lower rib cage (ground); bare wires were added for connectivity. After drying, the electrodes were connected in the Lead I configuration using an FDA-cleared physiological monitoring system (BIOPAC MP36). ECG data was collected from the Ag dry electrodes for 30 minutes. Next, three Ag/AgCl conventional electrodes (3M Red Dot) were adhered next to the Ag ink electrodes. An additional 30 minutes of data was collected from disposable Ag/AgCl electrodes

in the same configuration. Both datasets were filtered in MATLAB using a Butterworth 4th order low-pass filter with the cut-off frequency set to 30 Hz.

Sections of both ECG datasets are provided in **Figure 5.5**. Comparison of the PQRS waves from the two datasets showed negligible feature distortion. This suggested that the Ag ink-based dry electrodes were sufficiently conductive while also maintaining skin contact comparable to the Ag/AgCl wet electrodes. From this experiment, it was inferred that the Ag ink could attain excellent skin conformity and physiological signals with good fidelity to conventional equivalents.

5.3.2 Electrodermal activity

Electrodermal activity (EDA) is a component of lie detection that picks up changes in skin conductivity due to sweat production. For this reason, conformal dry electrodes are also beneficial to EDA.[115] From a user standpoint, the main difference is setup. While ECG electrodes are placed across the heart, EDA electrodes are placed on the fingertips and other areas of the body that contain high densities of sweat glands. A current is passed through two proximal locations (e.g. two fingers); the conductivity measurement is the EDA.

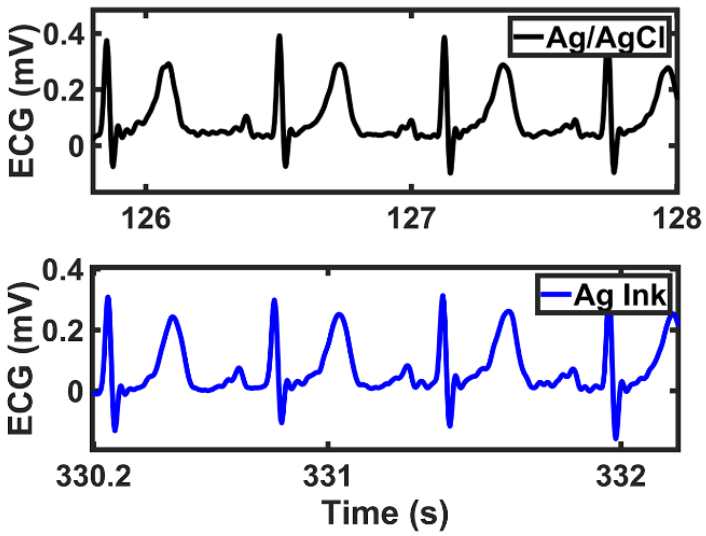

Figure 5.5 Comparison of ECG data collected from the Ag/AgCl conventional electrodes (top) versus the Ag ink electrodes (bottom).

EDA was chosen as the next type of physiological to test due to sharing similar concerns with ECG. For this reason, the experimental setup incorporated both ECG and EDA monitoring. To test the efficacy of the Ag dry electrodes for EDA, the subject underwent a Stroop task. The subject identified paranormal fright and video games as sources of cognitive stress, therefore a play-by-play video stream reviewing a Halloween game was prepared. In this experiment, the Ag ink dry electrodes for ECG were painted on the hands and left leg in a Lead II configuration. Ag ink dry electrodes for EDA were painted onto the distal phalanges of the left index and middle fingers. (Alternatively, Ag ink mixed with a small percentage of potassium chloride (KCl) could be used for EDA purposes.[133] The KCl increases the availability of chloride ions and also adds porosity to the electrode.) Reusable Ag/AgCl wet electrodes for EDA were adhered onto the medial phalanges of the left index and middle fingers (i.e. next to the Ag dry electrodes). All electrodes were connected to the BIOPAC physiological monitoring system.

At the start of the recording period, the subject was instructed to sit neutrally and passively listen to meditative music. This allowed the ECG and EDA electrodes to settle to baseline values. After 20 minutes, the meditative music was paused, and the subject was instructed to actively watch the full duration of the prepared video. After the video ended, the subject switched back to passive listening of meditative music.

Data from the Stroop task experiment is shown in **Figure 5.6**. The ECG electrodes were able to pick up clean PQRS waves from the Lead II configuration. However, during the active stressor period, motion artifacts were picked up whenever the subject involuntarily jerked away from the screen. These were observed to be a wire problem rather than the electrode itself. The interface between the connecting wire and the flexible dry electrode was susceptible to motion due to a stiffness mismatch.

For EDA, the Ag/AgCl wet electrodes and Ag ink dry electrodes appeared to exhibit inverse datasets. This was possibly due to placement since the distal phalanges undergo more sweat production than the medial phalanges. Based on the signal magnitude, the Ag ink dry electrodes were more conductive than the Ag/AgCl wet electrodes, suggesting an advantage of using dry electrodes for sweat conductivity measurements. Comparing the baseline and stress trigger periods also showed that the Ag ink dry electrodes exhibited a greater change in magnitude compared to the Ag/AgCl wet electrodes. This added sensitivity to cognitive stress and associated sweat production remains to be explored.

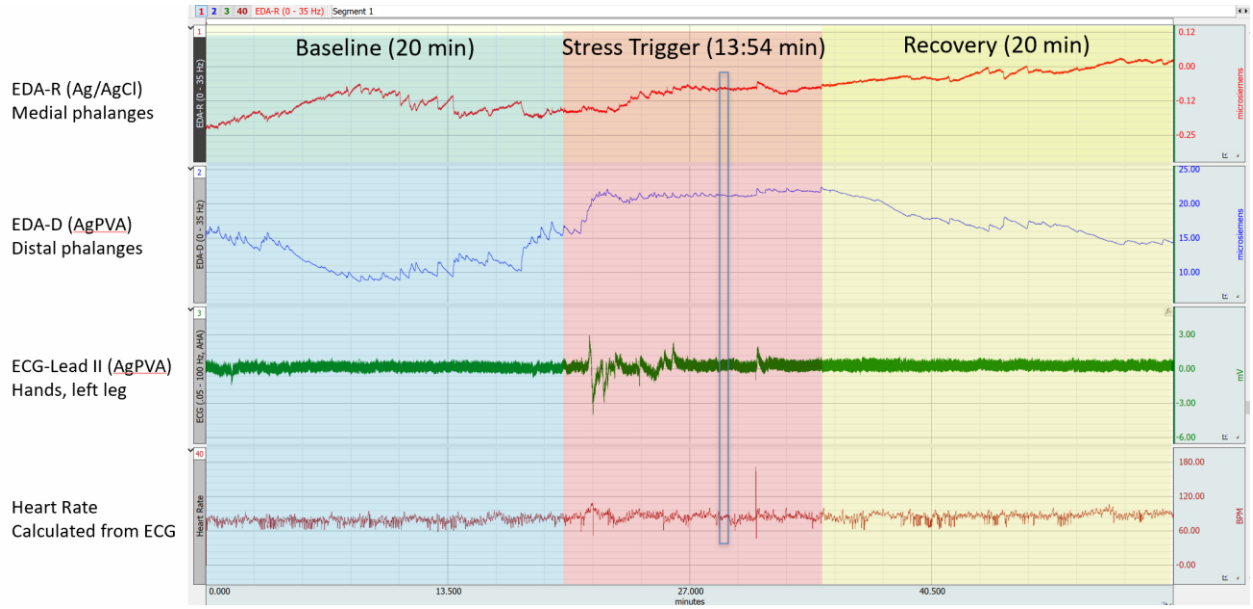

Figure 5.6 ECG and EDA data collected from a Stroop cognitive stressor task (video). The trigger was applied after a 20-min baseline period, followed by a 20-min recovery period. The spikes observed in the stressor period were due to involuntary motion.

5.4 Wireless multi-layer devices

5.4.1 Wireless design

The strategy for achieving wireless data transmission with the Ag ink involved patterning resonant coils that could operate standalone or incorporated into other sensor designs. Prior work by the collaborators of this work included wireless biosensing with miniaturized footprints to mount onto teeth.[15,16] To test for resonance in Ag ink, resonant coil designs factored the number of turns, coil width, and radial pitch necessary to minimize resistive losses for optimal device resonance and sensitivity in the form of a peak quality factor (Q). Modelling and optimization of these design parameters were performed computationally on COMSOL to tune the Ag coils to operate at radiofrequency (RF) or near-field communication (NFC) ranges. Once a working design was reached, 90-um thick Ag inductive coils were patterned onto glass slides for support. This thickness was chosen for its mechanical stability. Thinner films were more brittle while thicker films were more likely to delaminate from the skin. The coils were tested using a vector network analyzer (VNA, Keysight Technologies 53063A).

Figure 5.7 reports the resonance data collected from the Ag coils within two (2) 2.5 mm-wide turns and a radial pitch of 3.5 mm. For this specific design, resonance was observed at resistance values below 100 Ω and produced a sharp peak at ~ 5 Ω, suggesting that a benchmark resistance value of 10 Ω was necessary to optimize the quality factor Q. Since the Ag coils were able to elicit sharp resonance peaks, it was determined that the Ag ink was sufficiently conductive for manufacturing sensors with wireless capabilities.

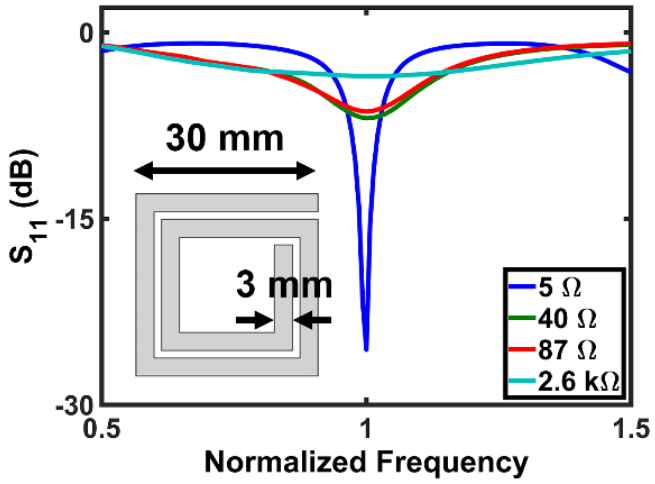

Figure 5.7 Resonance of Ag ink coils. Magnitude of the resonance peak versus electrical resistance of the Ag coil as measured on the VNA.

To fabricate wireless pressure sensors, a multilayer approach was used. Sequential conductive layers were prepared in advance on PDMS membranes or polyurethane bandages. A hole exposing the design terminal of the lower conductive layer was cut next to the sequential layer's terminal. After layer placement, the terminals of the coil designs were electrically bridged via addition of thin drops of Ag ink.

5.4.2 Pressure sensor

Wireless pressure sensors were fabricated using the multilayer approach. The capacitive based pressure sensors consisted of two Ag layers sandwiching a dielectric interlayer. The top and bottom Ag layers were mirror images that formed an RF resonator when electrically connected at their coil terminals. Each layer contained a two-turn inductive coil connected to a central capacitive plate. Five interlayer materials were tested: 0.5 mm-thick and 1 mm-thick Qgel silicone; 0.5 mm-thick and 1 mm-thick Ecoflex silicone; and Tegaderm polyurethane tape. One (1) mm-thick Qgel interlayers were found to produce the most sensitive sensors with larger detected pressure ranges due to their dielectric permittivity, flexibility, and greater compressibility.

Figure 5.8A shows a schematic image of the pressure sensor along with an image of the actual sensor mounted on the wrist. The fundamental response of the RF resonator as a pressure

sensor was modelled using a series RLC equivalent circuit. The variable capacitor of the circuit represented the variation in sensor capacitance due to interlayer flattening from applied pressure. To characterize pressure sensitivity, the sensors underwent *ex-vivo* (**Figure 5.8B-C**) and *in-vivo* (**Figure 5.8E-F**) loading/unloading experiments that elicited resonant frequency shifts. The resonant frequency of the S_{11} response was found to decrease with increasing pressure on the parallel plate capacitive region. Specifically, 50 Pa of applied pressure resulted in a resonant frequency shift of approximately 4%. The sensor response time was calculated as the time difference between the loaded incremental aliquots and registered resonant frequency changes on the VNA. Based on footage of the *ex-vivo* taken at 29.97 frames/s, the empirical response time was < 701 ms. This value was dependent on the refresh rate of the VNA display, which is not specified by the equipment manufacturer. Therefore, the actual response time is expected to be less and competitive against other pressure sensors.[103]

The pressure sensors were found to be highly repeatable in its linear operating range for both the *ex-vivo* and *in-vivo* experiments (**Figure 5.8D**), making them compatible for long-term skin wearability. The *in-vivo* loading/unloading experiments were performed at higher pressure values to bypass the hysteresis observed in the *ex-vivo* tests. Like the *ex-vivo* results, *in-vivo* pressure application caused the resonant frequency to downshift, but with less observed hysteresis as expected. This suggests that the current wireless sensor design has an optimal pressure range above 50 Pa.

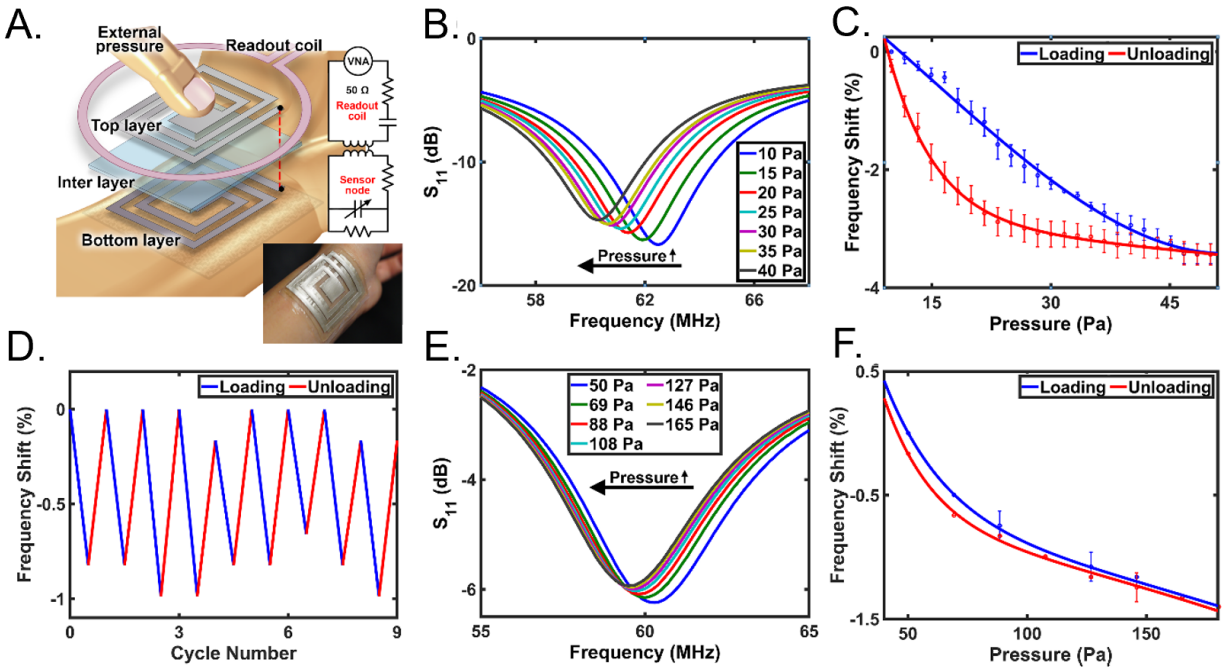

Figure 5.8 Multilayer wireless Ag pressure sensor. A) Schematic of the sensor with a central parallel plate capacitive region and outer inductive loops. Red dotted line represents the electrical bridge. Inset is the actual pressure sensor mounted onto the wrist. B) Effect on resonant frequency from applied pressure. C) *Ex-vivo* loading and unloading test. D) *Ex-vivo* repeatability test. E) *In-vivo* loading and unloading test performed on the wrist. F) *In-vivo* repeatability test.

The pressure sensors were also tested *ex-vivo* and *in-vivo* for sensitivity from a proximal finger (a known parasitic capacitive source). The finger initially contacted the center of the sensor without applying pressure, and then incrementally moved further away until frequency perturbations were no longer observed. Plots of the S11 frequency shift versus distance are provided in **Figure 5.9**. The finger was calculated to contribute a maximal resonant frequency shift of 1.5% *ex-vivo* and 3% *in-vivo*. Frequency shifts in the *in-vivo* conditions were more prominent within 0.5 mm distance. Beyond that distance, the profile of the frequency shift closely mimicked the *ex*-vivo condition. Notably, both conditions did not elicit a frequency shift until the finger was less than 1.5 mm away from the pressure sensor. Given the small distance and low resonant frequency shift, the effects of moving limbs are relatively small.

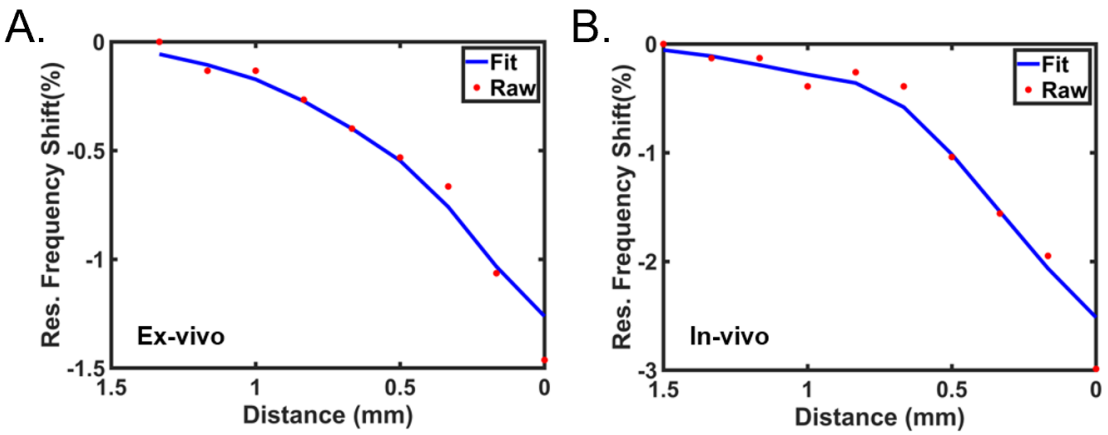

Figure 5.9 Characterization of parasitic capacitance. Resonant frequency shift is caused by a finger approaching the pressure sensor under A) *ex-vivo* and B) *in-vivo* conditions.

5.4.3 NFC linkage for power delivery

To demonstrate battery-free capabilities via NFC linkage, two-layer Ag receiving resonators (Rx) were interfaced with low-profile LEDs (see **Figure 5.10A** for schematic illustration and placement of LEDs); transmitting resonators (Tx) were interfaced with surface mount devices (SMDs). Components were homogenously connected via using the Ag ink as conductive glue. The resulting Rx resonators were capable of being powered by the NFC signal transmitted from a smartphone. **Figure 5.10B** shows the relationship between the luminosity of the attached red LEDs and the distance of the Rx resonator from the smartphone. The luminosity was observed to be consistent 0-10 mm distance from the smartphone, followed by a linear decline until the LED was no longer visibly lit at ~20 mm distance. The transmission loss was found to be approximately -30 dB within NFC ranges, which is sufficient for low-powered chip components. Green LEDs with comparatively higher current ratings were also successfully powered by the NFC smartphone linkage (**Figure 5.10C**). The NFC linkage can potentially supply power to more demanding chip components such as the portable diodes found in photoplethysmography sensors.

Modelling of the coupling coefficient suggested that the electromagnetic field was most substantial when two identical Ag resonators were within 2 mm apart (**Figure 5.10D**). To empirically test, pre-assembled multilayer resonators with polyurethane interlayers were laminated onto the palms of Hands A (Rx) and B (Tx). The resonator on Hand A was interfaced with a red LED while Hand B was connected to a power supply set within the NFC operating range. After lamination, both resonators were insulated with coatings of spray-on liquid bandage material (3M Nexcare). The liquid bandage was able to flex with hand motion and provide moisture protection for prolonged wear. Next, a peer-to-peer linkage was established in the form of a handshake. Upon entering the handshake, the LED illuminated when the Rx resonator was within 2 mm of the Tx resonator. The luminosity continued to increase until the hands were flush against each other. Repeated testing showed that the linkage was successful if the Rx and Tx resonators achieved at least 80% of their transversal and rotational alignment. Further optimization of the Ag ink formula and the resonator designs is expected to improve the wireless NFC link.

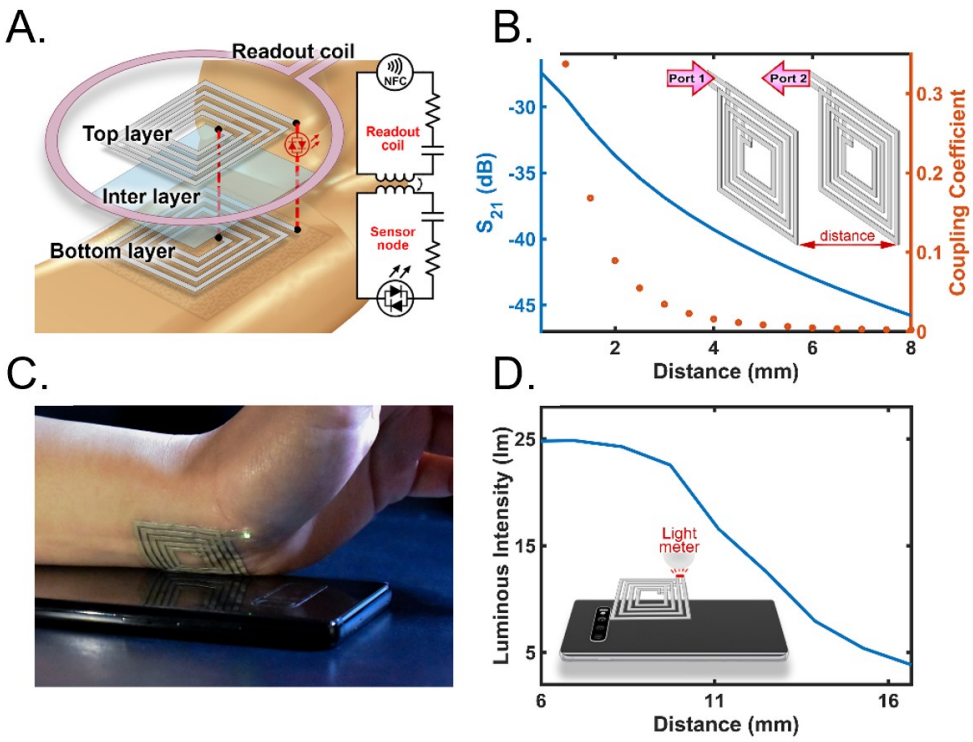

Figure 5.10 Multilayer Ag resonator for NFC linkage. A) Schematic of the layers and connections. Red lines represent the electrical bridges. The LEDs are positioned across the outer terminal. B) FEM modeling of the transmission efficiency and correlation coefficient. C) Demonstration of wireless power transmission from an NFC-enabled device. D) Luminosity of the red LEDs as a function of distance away from the NFC transmitter.

5.5 Summary

A simple formulation of Ag ink made from Elmer's Glue-All® was introduced and made into paint-on epidermal electronics and conductive temporary tattoos. Skin-like soft electronics made from the non-toxic conductive Ag ink demonstrated achievement of on-demand and configurable on-skin electronics manufacture. The ink achieved excellent epidermal contact and could withstand deformation within the 30% physiological range of skin strain. Conductive performance was attained using a lower concentration of Ag flakes compared to pre-existing ink formulas. The Ag flakes were stabilized using the commercially available PVA-based glue. The conductive ink was used to fabricate homogenous single- and multi-layer sensors and antennas

with standalone wireless capabilities as well as the option to incorporate commercial chip components (e.g. LEDs).[134] The sensors were demonstrated for their potential as *in vivo* wireless pressure sensors with high sensitivity and repeatability; and as smartphone-NFC linkage devices for wireless power delivery.

The investigation of children's school glue as a non-toxic stabilizer for conductive inks generated multiple positive discoveries. Foremost, the standalone glue formula was sufficient at stabilizing the suspended Ag flakes to form substantial conductive networks, making the two-ingredient recipe a simple and cost-effective material alternative in electronics development. The strategy of patterning wet ink onto the skin and air-drying allowed convenient scaling of skin-printable electronic designs for tailored applications and placement. It also allowed for seamless integration of wireless and battery-free capabilities into wearable sensors, bringing the public closer to smartphone-powered physiological monitors.

CHAPTER 6: Summary and future work

6.1 Summary of the work

In this work, conformal wearable electronics were developed with the vision for ubiquitous human physiological monitoring. Various factors of wearability and physiological sensing were improved to address the current shortcomings of portable and continuous vitals monitoring. For dynamic motion sensing, strain sensors were developed with enhanced stretchability and sensitivity to mechanical strain (Chapter 2). The sensors exhibited low hysteresis and latency suitable for high-resolution motion feedback control in low- and high-strain conditions. To demonstrate motion feedback, the strain sensors were used to generate digital models of finger and knee joint motion for rehabilitative feedback (Chapter 3). To demonstrate their clinical relevance, a system of conformal soft electronics was used to collect continuous biometric data (Chapter 4). The pilot study on CHF tested on patients with medical impairment and compared their biometric to age and gender-correlated healthy subjects. Respiration patterns and beat-to-beat variability of blood pressure and heart rate correlated with the CHF prognosis, suggesting their potential as digital biomarkers for early detection of CHF or disease management. Another pilot study extracted hemodynamic parameters of the beat-to-beat blood pressure data for assessing CVD risk and endothelial health. To address skin conformity for extended monitoring needs, a non-toxic conductive silver ink was developed using Elmer's school glue (Chapter 5). Paint-on electrodes achieved excellent skin contact for high quality ECG and EDA measurements without the need for hydrogel interlayers. To meet portability demands, the conductive silver ink was used to make temporary tattoo-like wireless sensors. By using the conductive ink as glue, multi-layer sensors were fabricated without concern for interconnecting failure points. Lastly, a demonstration of NFC

linkage to power LEDs addressed the desire for battery-free operation of wearable devices, which is crucial for convenience and low-profile wear.

Experimental studies involving human subject research were conducted under the approval of the Institutional Review Board (IRB) at UC Irvine.

6.2 Concluding remarks

Many challenges of wearable electronics have addressed by incrementally improving the major factors affecting wearability and sensing. Highly stretchable electronics were fabricated on thermoplastic platforms with greater shrinkage. Depending on the functional material choice, the resulting electronics were optimized for strain sensitivity or low electrical resistance. Early iterations of epidermal electronics introduced strain-relieving geometries and soft support materials to closely match the flexibility and stretchability of skin.[20] But they were predominantly developed for low-mobility sensing needs (e.g. ECG and other electrophysical data). To fully mimic the dynamic properties of the body, greater stretchability over the joints was necessary. The strain sensors were demonstrated to withstand high strain on the finger and knee joints while providing high-resolution measurements. With the shrink-induced wrinkles, the sensors also possess high surface area. The sensors could be manipulated to utilize their high surface area, e.g. lower limits of biomarker detection for point-of-care applications.

Existing wearable electronics for physiological monitoring operate as standalone devices with high barriers against central integration. Individual components can record and analyze specific categories of biometric data. But a comprehensive system of monitors that can intercommunicate enable the analysis of multi-variable data, which is particularly useful for disease detection and management. The respiration and blood pressure monitors, in conjunction

with other commercially available devices, were used to assess biometric data from CHF and healthy patients. Multiple variables and parameters were analyzed for their relevance as digital biomarkers for CVD. The joint force of respiration and blood pressure monitoring enabled the analysis of cardiopulmonary interdependent variables. If other types of sensors are incorporated, comprehensive vitals monitoring can be applied to more complex disease models.

Device development is often hindered by limitations in manufacturing and scalability. Roll-to-roll manufacturing has been used to scale the production of shrink-induced wrinkled thin films.[35] But large-scale manufacturing relies on pre-determined designs, which offers little versatility for downstream geometric considerations. Skin-safe conductive inks add design fluidity for on-demand, rapid manufacture of paint-on electronics. The ink's high conductivity qualifies it for wireless and battery-free electronics based on RF and NFC resonance. Utilizing a temporary tattoo format, the silver ink electronics can be built into body area networks for wider computing and monitoring needs. Finally, shelf-stable formula made from PVA-based Elmer's school glue addresses the implicit need for affordable access to wearable electronics in under-resourced regions.

The combination of these achievements will benefit future development of conformal wearable devices towards ubiquitous monitoring capabilities.

References

1. Heikenfeld, J. *et al.* Wearable sensors: modalities, challenges, and prospects. *Lab Chip* **18**, 217–248 (2018).
2. Asada, H. H. & Reisner, A. Wearable sensors for human health monitoring. in *Smart Structures and Materials 2006: Sensors and Smart Structures Technologies for Civil, Mechanical, and Aerospace Systems* (eds. Tomizuka, M., Yun, C.-B. & Giurgiutiu, V.) **6174**, 617401 (SPIE, 2006).
3. Marazzi, G. *et al.* Comparison of Microlife BP A200 Plus and Omron M6 blood pressure monitors to detect atrial fibrillation in hypertensive patients. *Adv. Ther.* **29**, 64–70 (2012).
4. Wilhelm, F. H., Roth, W. T. & Sackner, M. A. The LifeShirt. *Behav. Modif.* **27**, 671–691 (2003).
5. Diaz, K. M. *et al.* Fitbit®: An accurate and reliable device for wireless physical activity tracking. *Int. J. Cardiol.* **185**, 138–140 (2015).
6. Fallahzadeh, R., Pedram, M. & Ghasemzadeh, H. SmartSock: A wearable platform for context-aware assessment of ankle edema. *Proc. Annu. Int. Conf. IEEE Eng. Med. Biol. Soc. EMBS* **2016-Octob**, 6302–6306 (2016).
7. Wang, S. *et al.* Mechanics of Epidermal Electronics. *J. Appl. Mech.* **79**, 031022 (2012).
8. Yeo, W. H. *et al.* Multifunctional epidermal electronics printed directly onto the skin. *Adv. Mater.* **25**, 2773–2778 (2013).
9. Pegan, J. D. *et al.* Skin-mountable stretch sensor for wearable health monitoring. *Nanoscale* **8**, 17295–17303 (2016).
10. Pilditch, R. L., Lizardi, I., Nelson, B. C. & Johnson, M. M. SKIN-SAFE CONDUCTIVE INK AND METHOD FOR APPLICATION ON THE BODY. (2012).
11. Tian, B., Liu, Q., Luo, C., Feng, Y. & Wu, W. Multifunctional Ultrastretchable Printed Soft Electronic Devices for Wearable Applications. *Adv. Electron. Mater.* **6**, 1900922 (2020).
12. Guo, R. *et al.* Semi-Liquid-Metal-(Ni-EGaIn)-Based Ultraconformable Electronic Tattoo. *Adv. Mater. Technol.* **4**, 1900183 (2019).
13. Kim, J. *et al.* Soft Wearable Pressure Sensors for Beat-to-Beat Blood Pressure Monitoring. *Adv. Healthc. Mater.* **8**, 1900109 (2019).
14. Chu, M. *et al.* Respiration rate and volume measurements using wearable strain sensors. *npj Digit. Med.* **2**, 8 (2019).
15. Tseng, P., Napier, B., Garbarini, L., Kaplan, D. L. & Omenetto, F. G. Functional, RF-Trilayer Sensors for Tooth-Mounted, Wireless Monitoring of the Oral Cavity and Food Consumption. *Adv. Mater.* **30**, 1703257 (2018).
16. Dautta, M., Alshetaiwi, M., Escobar, J. & Tseng, P. Passive and wireless, implantable glucose sensing with phenylboronic acid hydrogel-interlayer RF resonators. *Biosens. Bioelectron.* **151**, 112004 (2020).
17. Berry, M. *et al.* Prognostic value of systolic short-term blood pressure variability in systolic heart failure. *Clin. Hypertens.* **22**, 16 (2016).
18. Mortara, A. *et al.* Abnormal awake respiratory patterns are common in chronic heart failure and may prevent evaluation of autonomic tone by measures of heart rate variability. *Circulation* **96**, 246–252 (1997).
19. Gibelin, P., Spillner, E., Bonnan, S. & Chevallier, T. Non-invasive blood pressure variability in chronic heart failure: characteristics and prognostic value. *Arch. Mal. Coeur*

Vaiss. **96**, 955–62 (2003).
20. Kim, D. H. *et al.* Epidermal electronics. *Science (80-.).* **333**, 838–843 (2011).
21. Li, R. T. *et al.* Wearable Performance Devices in Sports Medicine. *Sport. Heal. A Multidiscip. Approach* **8**, 74–78 (2016).
22. Yamada, T. *et al.* A stretchable carbon nanotube strain sensor for human-motion detection. *Nat. Nanotechnol.* **6**, 296–301 (2011).
23. Gibbs, P. T. & Asada, H. H. Wearable Conductive Fiber Sensors for Multi-Axis Human Joint Angle Measurements. *J. Neuroeng. Rehabil.* **2**, 7 (2005).
24. Lin, S., Lee, E. K., Nguyen, N. & Khine, M. Thermally-induced miniaturization for micro- and nanofabrication: progress and updates. *Lab Chip* **14**, 3475–88 (2014).
25. Chi-Cheng Fu, B. *et al.* Tunable Nanowrinkles on Shape Memory Polymer Sheets. *Adv. Mater* **21**, 1–5 (2009).
26. Wei, H. *et al.* 3D Printing of Free-Standing Stretchable Electrodes with Tunable Structure and Stretchability. *Adv. Eng. Mater.* **19**, 1700341 (2017).
27. Zhu, Y. & Moran-Mirabal, J. Highly Bendable and Stretchable Electrodes Based on Micro/Nanostructured Gold Films for Flexible Sensors and Electronics. *Adv. Electron. Mater.* **2**, 1500345 (2016).
28. Kim, J. *et al.* Highly stretchable wrinkled gold thin film wires. *Appl. Phys. Lett.* **108**, (2016).
29. Park, S.-J., Kim, J., Chu, M. & Khine, M. Highly Flexible Wrinkled Carbon Nanotube Thin Film Strain Sensor to Monitor Human Movement. *Adv. Mater. Technol.* **1**, 1600053 (2016).
30. Pikula, K. S. *et al.* Effects of carbon and silicon nanotubes and carbon nanofibers on marine microalgae Heterosigma akashiwo. *Environ. Res.* **166**, 473–480 (2018).
31. Larimi, S. R. *et al.* Low-cost ultra-stretchable strain sensors for monitoring human motion and bio-signals. *Sensors Actuators A Phys.* **271**, 182–191 (2018).
32. Khosla, A., Furukawa, H. & Sukumaran, S. K. Resistive Hysteresis of Carbon Nanofiber Doped Elastomeric Nanocomposite Polymer. *Meet. Abstr.* **MA2017-02**, 2116–2116 (2017).
33. Cho, D. *et al.* Three-Dimensional Continuous Conductive Nanostructure for Highly Sensitive and Stretchable Strain Sensor. *ACS Appl. Mater. Interfaces* **9**, 17369–17378 (2017).
34. Lin, L., Chu, M., Park, S., Zakashansky, J. A. & Khine, M. Conformal Stretch Sensors for High Resolution Motion Sensing and Control. *Macromol. Mater. Eng.* **304**, 1800520 (2019).
35. Nokes, J. M. *et al.* Reduced Blood Coagulation on Roll-to-Roll, Shrink-Induced Superhydrophobic Plastics. *Adv. Healthc. Mater.* **5**, 593–601 (2016).
36. Nguyen, D. *et al.* Better shrinkage than Shrinky-Dinks †. doi:10.1039/c001082k
37. Sharac, N. *et al.* Tunable optical response of bowtie nanoantenna arrays on thermoplastic substrates. *Nanotechnology* **27**, 105302 (2016).
38. Lin, S., Hedde, P. N., Venugopalan, V., Gratton, E. & Khine, M. Multi-scale silica structures for improved HIV-1 Capsid (p24) antigen detection. *Analyst* **141**, 4181–4188 (2016).
39. Pegan, J. D., Ho, A. Y., Bachman, M. & Khine, M. Flexible shrink-induced high surface area electrodes for electrochemiluminescent sensing. *Lab Chip* **13**, 4205 (2013).
40. Hauke, A. *et al.* Superwetting and aptamer functionalized shrink-induced high surface

area electrochemical sensors. *Biosens. Bioelectron.* **94**, 438–442 (2017).
41. Freschauf, L. R., Mclane, J., Sharma, H. & Khine, M. Shrink-Induced Superhydrophobic and Antibacterial Surfaces in Consumer Plastics. *PLoS One* **7**, 40987 (2012).
42. Nokes, J. *et al.* Nanotextured Shrink Wrap Superhydrophobic Surfaces by Argon Plasma Etching. *Materials (Basel).* **9**, 196 (2016).
43. Pawlaczyk, M., Lelonkiewicz, M. & Wieczorowski, M. Age-dependent biomechanical properties of the skin. *Postepy Dermatologii i Alergologii* **30**, 302–306 (2013).
44. Seghir, R. & Arscott, S. Extended PDMS stiffness range for flexible systems. *Sensors Actuators, A Phys.* **230**, 33–39 (2015).
45. Kaminsky, W. Trends in polyolefin chemistry. *Macromol. Chem. Phys.* **209**, 459–466 (2008).
46. Huang, Y. *et al.* Microfluidic serpentine antennas with designed mechanical tunability. *Lab Chip* **14**, 4205–4212 (2014).
47. Atalay, O. *et al.* A Highly Stretchable Capacitive-Based Strain Sensor Based on Metal Deposition and Laser Rastering. *Adv. Mater. Technol.* **2**, 1700081 (2017).
48. Soucie, J. M. *et al.* Range of motion measurements: Reference values and a database for comparison studies. *Haemophilia* **17**, 500–507 (2011).
49. Kumar, D., Manal, K. T. & Rudolph, K. S. Knee joint loading during gait in healthy controls and individuals with knee osteoarthritis. *Osteoarthr. Cartil.* **21**, 298–305 (2013).
50. Shultz, S. J., Carcia, C. R. & Perrin, D. H. Knee joint laxity affects muscle activation patterns in the healthy knee. *J. Electromyogr. Kinesiol.* **14**, 475–483 (2004).
51. Millett, P. J., Wickiewicz, T. L. & Warren, R. F. Motion loss after ligament injuries to the knee: Part i: Causes. *Am. J. Sports Med.* **29**, 664–675 (2001).
52. Poomsalood, S., Muthumayandi, K. & Hambly, K. Can stretch sensors measure knee range of motion in healthy adults? *Biomed. Hum. Kinet.* **11**, 1–8 (2019).
53. Chu, M. *et al.* Respiration rate and volume measurements using wearable strain sensors. *npj Digit. Med.* **2**, (2019).
54. O'driscoll, S. W. & Giori, N. J. *Continuous passive motion (CPM) : Theory and principles of clinical application*. *Journal of Rehabilitation Research and Development* **37**,
55. Lin, L. I.-K. A Concordance Correlation Coefficient to Evaluate Reproducibility. *Biometrics* **45**, 255 (1989).
56. Dickinson, J. A., Cook, S. D. & Leinhardt, T. M. The measurement of shock waves following heel strike while running. *J. Biomech.* **18**, 415–422 (1985).
57. Bible, J. E., Simpson, A. K., Biswas, D., Pelker, R. R. & Grauer, J. N. Actual knee motion during continuous passive motion protocols is less than expected. *Clin. Orthop. Relat. Res.* **467**, 2656–2661 (2009).
58. Dias, D. & Cunha, J. P. S. Wearable health devices—vital sign monitoring, systems and technologies. *Sensors (Switzerland)* **18**, (2018).
59. Peake, J. M., Kerr, G. & Sullivan, J. P. A Critical Review of Consumer Wearables, Mobile Applications, and Equipment for Providing Biofeedback, Monitoring Stress, and Sleep in Physically Active Populations. *Front. Physiol.* **9**, 743 (2018).
60. Taj-Eldin, M., Ryan, C., O'flynn, B. & Galvin, P. A review of wearable solutions for physiological and emotional monitoring for use by people with autism spectrum disorder and their caregivers. *Sensors (Switzerland)* **18**, (2018).
61. Sampson, M. *et al. CONTINUOUS TEMPERATURE MONITORING IN THE INPATIENT SETTING USING TEMPTRAQ*.

62. Johnston, E. D. *et al.* Oxygen targeting in preterm infants using the Masimo SET Radical pulse oximeter. *Arch. Dis. Child. Fetal Neonatal Ed.* **96**, 429–433 (2011).
63. Volterrani, M., Spoletini, I., Angermann, C., Rosano, G. & Coats, A. J. Implantable devices for heart failure monitoring: The CardioMEMS^{TM} system. *Eur. Hear. Journal, Suppl.* **21**, M50–M53 (2019).
64. ClearSight System. *Edwards Lifesciences Corporation* (2019). Available at: https://www.edwards.com/gb/devices/Hemodynamic-Monitoring/clearsight. (Accessed: 30th April 2019)
65. Xu, J., Murphy, S. L., Kochanek, K. D. & Arias, E. *Mortality in the United States, 2018 Key findings Data from the National Vital Statistics System*. (2018).
66. Garcia, J. E. & Wright, V. R. *Congestive heart failure : Symptoms, Causes and Treatment*. (Nova Science Publishers, 2010).
67. Bui, A. L., Horwich, T. B. & Fonarow, G. C. Epidemiology and risk profile of heart failure. *Nat. Rev. Cardiol.* **8**, 30 (2011).
68. Center, W. S. Heart Failure Statistics. *Emory Healthc.* 1–2 (2016).
69. Mozaffarian, D. *et al.* Heart Disease and Stroke Statistics—2016 Update. *Circulation* **133**, (2016).
70. Hall, M. J., Levant, S. & DeFrances, C. J. Hospitalization for congestive heart failure: United States, 2000-2010. *NCHS Data Brief* 1–8 (2012).
71. Ho, K. K., Anderson, K. M., Kannel, W. B., Grossman, W. & Levy, D. Survival after the onset of congestive heart failure in Framingham Heart Study subjects. *Circulation* **88**, 107–15 (1993).
72. American Heart Association. Warning Signs of Heart Failure. (2015).
73. Sheifer, S. E. *et al.* Time to presentation with acute myocardial infarction in the elderly: associations with race, sex, and socioeconomic characteristics. *Circulation* **102**, 1651–1656 (2000).
74. Wilhelmsen, L., Eriksson, H., Svardsudd, K. & Caidahl, K. Improving the detection and diagnosis of congestive heart failure. *Eur. Heart J.* **10**, 13–18 (1989).
75. Suh, M. K. *et al.* A remote patient monitoring system for congestive heart failure. in *Journal of Medical Systems* **35**, 1165–1179 (2011).
76. Iravantchi, Y., Gajos, K. Z., Grosz, B. & Link, C. SwellFit : a Wearable Sensor for Patients with Congestive Heart Failure The Harvard community has made this article openly available . Accessed SwellFit : a Wearable Sensor for Patients with Congestive Heart Failure. (2017).
77. Kim, J. *et al.* Soft Wearable Pressure Sensors for Beat-to-Beat Blood Pressure Monitoring. *Adv. Healthc. Mater.* **8**, 1900109 (2019).
78. Højgaard, M. V., Holstein-Rathlou, N.-H., Agner, E. & Kanters, J. K. Dynamics of spectral components of heart rate variability during changes in autonomic balance. *Am. J. Physiol. Circ. Physiol.* **275**, H213–H219 (1998).
79. Parati, G., Ochoa, J. E. & Bilo, G. Blood Pressure Variability, Cardiovascular Risk, and Risk for Renal Disease Progression. *Curr. Hypertens. Rep.* **14**, 421–431 (2012).
80. Parati, G., Ochoa, J. E., Lombardi, C. & Bilo, G. Assessment and management of blood-pressure variability. *Nat. Rev. Cardiol.* **10**, 143–155 (2013).
81. Jackson, G., Gibbs, C. R., Davies, M. K. & Lip, Y. H. ABC of Heart Failure: Pathophysiology. *BMJ* **320**, 15 (2000).
82. Asyali, M. H. Discrimination power of long-term heart rate variability measures. in

Proceedings of the 25th Annual International Conference of the IEEE Engineering in Medicine and Biology Society (IEEE Cat. No.03CH37439) 200–203 (IEEE). doi:10.1109/IEMBS.2003.1279568
83. Umetani, K., Singer, D. H., McCraty, R. & Atkinson, M. Twenty-Four Hour Time Domain Heart Rate Variability and Heart Rate: Relations to Age and Gender Over Nine Decades. *J. Am. Coll. Cardiol.* **31**, 593–601 (1998).
84. Khayat, R. *et al.* Sleep-Disordered breathing in heart failure: Identifying and treating an important but often unrecognized comorbidity in heart failure patients. *Journal of Cardiac Failure* **19**, 431–444 (2013).
85. Diaphragmatic Breathing Retraining in Heart Failure Patients: Health-Behavior Related Outcomes - Full Text View - ClinicalTrials.gov. Available at: https://clinicaltrials.gov/ct2/show/NCT01478932. (Accessed: 15th December 2020)
86. Lieber, C. & Mohsenin, V. Cheyne-Stokes respiration in congestive heart failure. *Yale J. Biol. Med.* **65**, 39–50 (1992).
87. Brack, T. *et al.* Daytime Cheyne-Stokes Respiration in Ambulatory Patients With Severe Congestive Heart Failure Is Associated With Increased Mortality. *Chest* **132**, 1463–1471 (2007).
88. Mikael, L. de R. *et al.* Vascular Aging and Arterial Stiffness. *Arq. Bras. Cardiol.* **109**, 253–258 (2017).
89. Millasseau, S. C., Kelly, R. P., Ritter, J. M. & Chowienczyk, P. J. Determination of age-related increases in large artery stiffness by digital pulse contour analysis. *Clin. Sci. (Lond).* **103**, 371–7 (2002).
90. Raitakari, O. T. & Celermajer, D. S. Testing for endothelial dysfunction. *Annals of Medicine* **32**, 293–304 (2000).
91. Faulx, M. D., Wright, A. T. & Hoit, B. D. Detection of endothelial dysfunction with brachial artery ultrasound scanning. *American Heart Journal* **145**, 943–951 (2003).
92. Yang, Y. & Loscalzo, J. Regulation of Tissue Factor Expression in Human Microvascular Endothelial Cells by Nitric Oxide. *Circulation* **101**, 2144–2148 (2000).
93. Moerland, M. *et al.* Evaluation of the endoPAT as a tool to assess endothelial function. *Int. J. Vasc. Med.* **2012**, (2012).
94. EndoPAT® - Itamar Medical. Available at: https://www.itamar-medical.com/professionals/watchpat-300-copy/. (Accessed: 15th December 2020)
95. EndoPat® Reimbursement - Itamar Medical. Available at: https://www.itamar-medical.com/reimbursement/. (Accessed: 15th December 2020)
96. Chirinos, J. A. *et al.* Arterial wave reflections and incident cardiovascular events and heart failure: MESA (Multiethnic Study of Atherosclerosis). *J. Am. Coll. Cardiol.* **60**, 2170–2177 (2012).
97. Sá da Fonseca, L. J., Mota-Gomes, M. A. & Rabelo, L. A. Radial Applanation Tonometry as an Adjuvant Tool in the Noninvasive Arterial Stiffness and Blood Pressure Assessment. *World J. Cardiovasc. Dis.* **04**, 225–235 (2014).
98. Elgendi, M. On the analysis of fingertip photoplethysmogram signals. *Curr. Cardiol. Rev.* **8**, 14–25 (2012).
99. Mukhopadhyay, S. C. Wearable Sensors for Human Activity Monitoring: A Review. *IEEE Sens. J.* **15**, 1321–1330 (2015).
100. Liu, X., Vega, K., Maes, P. & Paradiso, J. A. Wearability factors for skin interfaces. in *ACM International Conference Proceeding Series* **25-27-February-2016**, (Association for

Computing Machinery, 2016).
101. Stoppa, M. & Chiolerio, A. Wearable Electronics and Smart Textiles: A Critical Review. *Sensors* **14**, 11957–11992 (2014).
102. Wu, W. Stretchable electronics: functional materials, fabrication strategies and applications. *Sci. Technol. Adv. Mater.* **20**, 187–224 (2019).
103. Kim, J. *et al.* Soft Wearable Pressure Sensors for Beat-to-Beat Blood Pressure Monitoring. *Adv. Healthc. Mater.* doi:10.1002/ADHM.201900109
104. Kim, J. *et al.* Miniaturized Battery-Free Wireless Systems for Wearable Pulse Oximetry. *Adv. Funct. Mater.* **27**, 1604373 (2017).
105. Orecchini, G., Yang, L., Tentzeris, M. M. & Roselli, L. Wearable battery-free active paper printed RFID tag with human-energy scavenger. in *IEEE MTT-S International Microwave Symposium Digest* (2011). doi:10.1109/MWSYM.2011.5972808
106. Han, S. *et al.* Battery-free, wireless sensors for full-body pressure and temperature mapping. *Sci. Transl. Med.* **10**, (2018).
107. Kumar, R. *et al.* All-Printed, Stretchable Zn-Ag $_2$ O Rechargeable Battery via Hyperelastic Binder for Self-Powering Wearable Electronics. *Adv. Energy Mater.* **7**, 1602096 (2017).
108. Bandodkar, A. J. *et al.* Epidermal tattoo potentiometric sodium sensors with wireless signal transduction for continuous non-invasive sweat monitoring. *Biosens. Bioelectron.* **54**, 603–609 (2014).
109. Xu, G. *et al.* Smartphone-based battery-free and flexible electrochemical patch for calcium and chloride ions detections in biofluids. *Sensors Actuators, B Chem.* **297**, 126743 (2019).
110. Xu, G. *et al.* Battery-Free and Wireless Epidermal Electrochemical System with All-Printed Stretchable Electrode Array for Multiplexed In Situ Sweat Analysis. *Adv. Mater. Technol.* **4**, 1800658 (2019).
111. Jeong, H. *et al.* Modular and Reconfigurable Wireless E-Tattoos for Personalized Sensing. *Adv. Mater. Technol.* **4**, 1900117 (2019).
112. Hajiaghajani, A., Kim, D., Abdolali, A. & Ahn, S. Patterned Magnetic Fields for Remote Steering and Wireless Powering to a Swimming Microrobot. *IEEE/ASME Trans. Mechatronics* **25**, 207–216 (2020).
113. O'Mahony, C. *et al.* Design, fabrication and skin-electrode contact analysis of polymer microneedle-based ECG electrodes. *J. Micromechanics Microengineering* **26**, 084005 (2016).
114. Chen, Y.-H. *et al.* Soft, Comfortable Polymer Dry Electrodes for High Quality ECG and EEG Recording. *Sensors* **14**, 23758–23780 (2014).
115. Posada-Quintero, H. F. *et al.* Novel dry electrodes for recording electrodermal activity. in *Proceedings of the Annual International Conference of the IEEE Engineering in Medicine and Biology Society, EMBS* **2016-October**, 5701–5704 (Institute of Electrical and Electronics Engineers Inc., 2016).
116. Chlaihawi, A. A., Narakathu, B. B., Emamian, S., Bazuin, B. J. & Atashbar, M. Z. Development of printed and flexible dry ECG electrodes. *Sens. Bio-Sensing Res.* **20**, 9–15 (2018).
117. Arquilla, K., Webb, A. & Anderson, A. Textile Electrocardiogram (ECG) Electrodes for Wearable Health Monitoring. *Sensors* **20**, 1013 (2020).
118. Venkata Krishna Rao, R., Venkata Abhinav, K., Karthik, P. S. & Singh, S. P. Conductive silver inks and their applications in printed and flexible electronics. *RSC Advances* **5**,

77760–77790 (2015).
119. Al-Halhouli, A., Qitouqa, H., Alashqar, A. & Abu-Khalaf, J. Inkjet printing for the fabrication of flexible/stretchable wearable electronic devices and sensors. *Sensor Review* **38**, 438–452 (2018).
120. Kay, R. & Desmulliez, M. A review of stencil printing for microelectronic packaging. *Soldering and Surface Mount Technology* **24**, 38–50 (2012).
121. Kamyshny, A. & Magdassi, S. Conductive Nanomaterials for Printed Electronics. *Small* **10**, 3515–3535 (2014).
122. Lin, L. *et al.* Paint-On Epidermal Electronics for On-Demand Sensors and Circuits. *Adv. Electron. Mater.* 2000765 (2020). doi:10.1002/aelm.202000765
123. Zhu, L., Wang, B., Handschuh-Wang, S. & Zhou, X. Liquid Metal–Based Soft Microfluidics. *Small* **16**, 1903841 (2020).
124. Faust, R. A. *TOXICITY SUMMARY FOR SILVER*. (1992).
125. Khansa, I., Schoenbrunner, A. R., Kraft, C. T. & Janis, J. E. Silver in Wound Care—Friend or Foe? *Plast. Reconstr. Surg. - Glob. Open* **7**, e2390 (2019).
126. Tian, B. *et al.* All-printed, low-cost, tunable sensing range strain sensors based on Ag nanodendrite conductive inks for wearable electronics. *J. Mater. Chem. C* **7**, 809–818 (2019).
127. Tian, B., Liu, Q., Luo, C., Feng, Y. & Wu, W. Multifunctional Ultrastretchable Printed Soft Electronic Devices for Wearable Applications. *Adv. Electron. Mater.* **6**, 1900922 (2020).
128. Luo, C., Tian, B., Liu, Q., Feng, Y. & Wu, W. One-Step-Printed, Highly Sensitive, Textile-Based, Tunable Performance Strain Sensors for Human Motion Detection. *Adv. Mater. Technol.* **5**, 1900925 (2020).
129. Zhu, Z. *et al.* 3D Printed Functional and Biological Materials on Moving Freeform Surfaces. *Adv. Mater.* **30**, 1707495 (2018).
130. Ershad, F. *et al.* Ultra-conformal drawn-on-skin electronics for multifunctional motion artifact-free sensing and point-of-care treatment. *Nat. Commun.* **11**, 1–13 (2020).
131. Lu, N., Lu, C., Yang, S. & Rogers, J. Highly Sensitive Skin-Mountable Strain Gauges Based Entirely on Elastomers. *Adv. Funct. Mater.* **22**, 4044–4050 (2012).
132. Kim, D. & Moon, J. Highly conductive ink jet printed films of nanosilver particles for printable electronics. *Electrochem. Solid-State Lett.* **8**, J30 (2005).
133. Posada-Quintero, H. F. *et al.* Dry carbon/salt adhesive electrodes for recording electrodermal activity. *Sensors Actuators, A Phys.* **257**, 84–91 (2017).
134. Dautta, M. *et al.* Multi-Functional Hydrogel-Interlayer RF/NFC Resonators as a Versatile Platform for Passive and Wireless Biosensing. *Adv. Electron. Mater.* **6**, 1901311 (2020).